The Structure of the Free Neutron at Large x-Bjorken

A 12 GeV Research Proposal to Jefferson Lab (PAC 36)

Resubmission of Conditionally Approved Experiment E12-06-113

M. Amarian, S. Bültmann (co-spokesperson)*, G. E. Dodge, C. E. Hyde, S. E. Kuhn (co-spokesperson), L. B. Weinstein

Old Dominion University, Norfolk, Virginia, USA

J. Arrington, R. Dupré, A. El Alaoui, K. Hafidi, X. Zhan

Argonne National Laboratory, Argonne, Illinois, USA

M. Battaglieri, R. De Vita

INFN Genova, Genova, Italy

N. Baillie, M. E. Christy (co-spokesperson), C. E. Keppel (co-spokesperson)

Hampton University, Hampton, Virginia, USA

J. C. Peng

University of Illinois at Urbana-Champaign, Urbana-Champaign, Illinois, USA

K. L. Giovanetti, G. Niculescu, I. Niculescu

James Madison University, Harrisonburg, Virginia, USA

N. Guler, A. Klein

Los Alamos National Laboratory, Los Alamos, New Mexico, USA

D. Dutta

Mississippi State University, Mississippi State, Mississippi, USA

H. Egiyan

University of New Hampshire, Durham, New Hampshire, USA

P.M. King

Ohio University, Athens, Ohio, USA

V. Tvaskis

University of Regina, Regina, Saskatchewan, Canada

S. Tkachenko

University of South Carolina, Columbia, South Carolina, USA

V. Burkert, A. Deur, R. Ent, H. Fenker (co-spokesperson),
W. Melnitchouk (co-spokesperson), S. Stepanyan, J. Zhang

Thomas Jefferson National Accelerator Facility, Newport News, Virginia, USA

N. Kalantarians

University of Virginia, Charlottesville, Virginia, USA

K. A. Griffioen (co-spokesperson)

The College of William and Mary, Williamsburg, Virginia, USA

and The CLAS Collaboration

* Contact: Stephen Bueltmann, Department of Physics, Old Dominion University, Norfolk, VA 23529. Email: sbueltma@odu.edu

Abstract

Understanding the structure of the nucleon is one of the fundamental goals of nuclear and high-energy physics. Deep-inelastic lepton scattering off proton and nuclear targets has produced a large amount of accurate data on the proton structure function, but not to the same extent on that of the neutron. Because of the instability of the free neutron, its structure is inferred from comparative measurements between nuclear targets, like deuterium, and proton targets. The precision of these measurements is limited because of the theoretical uncertainties introduced by nuclear models needed to extract information from the bound nucleons in the nuclei.

The BoNuS collaboration (experiment E03-012) measured the neutron structure in the Fall of 2005 by scattering electrons of up to 5.3 GeV energy on a thin deuterium gas target and detecting the low-momentum recoiling spectator protons in the vicinity of that target. By constraining the spectator proton to very low momenta and very backward scattering angles, electron scattering events on almost free neutrons could be selected.

We propose an extension of this measurement of the inclusive electron scattering cross section on an almost free neutron using the upgraded CEBAF Large Acceptance Spectrometer (CLAS12) and a modified recoil detector instead of the central silicon vertex detector. The recoil detector allows us to measure the momentum of the recoiling spectator proton down to about 70 MeV/c. This momentum measurement constrains the initial four-momentum of the scattered neutron in the reaction $D(e, e' p_s)X$ and, hence, enables us to select almost free neutrons.

We propose to use this technique to extract the structure function F_2^n at x from 0.1 up to 0.8 over a significant range in Q^2 (from about 1 to 14 GeV$^2/c^2$) and W from the nucleon mass, M, to 4.5 GeV with a beam energy of 11 GeV. CLAS12 will be used in its standard configuration with luminosities up to $2 \cdot 10^{34}$ cm^{-2}s^{-1}. We request a total of 42 days of new beamtime in Hall B (35 days at 11 GeV for the measurement on deuterium, five days of 11 GeV for the measurement on hydrogen, and two days at 11 GeV and lower energies for background studies and calibration runs).

Contents

1 Technical Participation of Research Groups

1.1 Old Dominion University

The Old Dominion University group is actively involved in this proposal, as well as several other proposal using CLAS12. Other members of our group are also pursuing a proposal for Hall A, but their contributions are not included here.

Among CLAS12 baseline equipment, the group was involved with the design and took the responsibility of prototyping the new drift chamber for CLAS12 and intends to take responsibility for the construction and testing of the Region 2 drift chambers. Five faculty, one postdoc, and one technician are working at least part time on this project in the next few years. Funding for the group is from DOE and from the university.

The university has provided a new building with office space and laboratories, including 3,000 square feet of high bay laboratory space with clean room capabilities for our use. A large clean room tent for the construction of the CLAS12 region 2 drift chambers has been built and is ready for use.

Beyond the baseline equipment, the group is also actively developing a new solid polarized target for CLAS12, with funding provided by a NSF MRI to a consortium of Christopher Newport University, the University of Virginia and ODU as the lead institution. The ODU group is also interested in exploring improvements to the BoNuS detector and a future RICH detector for CLAS12.

1.2 INFN Genova

The Genova group is actively involved with the CLAS12 upgrade program, in particular with the central detector. For the BoNuS12 experiment, the Genova group is contributing equipment and research time for the RTPC development, in particular for the DAQ system.

The Genova group presently owns electronic components of the RTPC readout system, purchased for the eg6 experiment in 2009.

1.3 Hampton University

Hampton University (HU) is actively involved in this proposal, as well as in the original BoNuS experiment. The group is also heavily involved in Hall C, where commitments have been made to build base equipment.

The HU group will continue to support development, augmentation, and use of the BoNuS target and detector system for 12 GeV in Hall B.

The HU nuclear experimental suite consists of over 1,400 square feet of lab space with an electronic lab station, mechanical lab station, computer/graphic processing bay and a dedicated radiation hot lab. The physics department, furthermore, has a 1,300 square foot class-10,000 clean room for component preparation and module construction.

Research support for the Hampton University nuclear experimental group comes predominantly from the National Science Foundation.

1.4 James Madison University

The James Madison University group is actively involved in this proposal, as well as other proposals using CLAS12. For the 12 GeV upgrade the group members are involved in building baseline equipment and associated infrastructure in both Hall B and C.

For CLAS12 JMU is part of the group that will build the preshower calorimeter. To this end an MOU with JLab was signed and NSF funding via an MRI was secured. The 1100 PMTs were acquired and tested in house and the resistive bases will be assembled starting in the Summer 2010.

The group is supported by a NSF RUI grant and has a strong undergraduate research component.

1.5 University of South Carolina

The University of South Carolina group is actively involved in the CLAS12 upgrade program, in particular with the development of the forward time of flight detector.

1.6 University of Virginia

The University of Virginia group is actively involved in the CLAS12 upgrade program, in particular with the development of the new polarized target.

1.7 The College of William and Mary

The College of William and Mary group is actively involved in this proposal, as well as several other proposals using CLAS12. Other members of our group are also pursuing a proposal for Hall A, but their contributions are not included here.

Among CLAS12 baseline equipment, the group is committed to building part of the preshower calorimeter, has signed an MOU with JLab to this effect, has secured NSF MRI funding, and is moving forward to begin cutting scintillators in Summer 2010. Two faculty members, several graduate students, a post-doctoral fellow, several undergraduates and at least two technicians are likely to work at least part time on this project. Funding for the group is from the DOE and the NSF.

Facilities at William and Mary include a 1000 sq. ft. clean room and a 2000 sq. ft. high bay suitable for detector construction and testing.

2 Introduction

We propose to use the "spectator tagging" technique to access the structure of the free neutron over a large range of values of Bjorken x, the fraction of the nucleon's momentum carried by the struck quark. It extends the program of neutron structure function measurements from the 5.3 GeV experiment E03-012 (BoNuS, or "Barely Off-shell NUcleon Structure", see Ref. [1]) to higher 4-momentum transfers squared, Q^2, and higher x, in the deep-inelastic scattering region, up to $x \approx 0.8$. The method involves detection of low momentum recoil protons with momenta down to 70 MeV/c in coincidence with high–energy electron scattering off deuterium.

The proposed experiment will study the structure of free neutrons with comparable detail and precision as has been achieved for the proton at the highest possible x values. For this goal, we will use a recoil detector, very similar to the radial time projection chamber (RTPC) built for the BoNuS experiment, but with twice the length and an extended radial drift region. The recoil detector will surround a thin deuterium target to "tag" scattering events on a nearly on-shell, loosely bound neutron by detecting slow protons emitted in the backward direction relative to the momentum transfer vector. Many other experiments will be possible with this apparatus, using other nuclear targets and/or detection of other nuclear fragments, exploring topics from the high–momentum structure of light nuclei to coherent production of mesons.

Structure functions of the nucleon reflect the defining features of QCD: asymptotic freedom at large momenta and small distance scales, as well as confinement and non-perturbative effects at the hadronic scale. From measurements of these structure functions in the scaling region, one can infer the momentum and spin carried by the quarks and (via perturbative evolution) the gluons inside the nucleon. At the same time, through scaling violations and $1/Q^2$ power corrections to the leading-twist structure functions, one gains access to the quark-gluon dynamics in a bound hadronic system. Finally, one can study the transition from quark to hadronic degrees of freedom through the phenomenon of duality.

After more than three decades of measurements at many laboratories worldwide, an impressive amount of data have been collected on the proton and the deuteron, extending over several orders of magnitude in x and Q^2. However, there are still regions of the kinematic phase space where data on the neutron are scarce or imprecise. A significant step towards filling these gaps was made by the BoNuS experiment E03-012 at 5.3 GeV, which measured the structure function of a nearly free neutron in the deep-inelastic region up to $x = 0.56$, at $Q^2 = 4$ (GeV/c)^2, and through the resonance region at higher x. Due to the lower energy available, E03-012 was not able to penetrate far into the deep-inelastic region. Jefferson Lab with an 11 GeV beam energy will for the first time allow one to reach values of x as high as $x \approx 0.85$ for $W > 1.8$ GeV and $x \approx 0.8$ in the deep-inelastic region above $W > 2$ GeV.

One of the most interesting open questions about the behavior of the structure functions is what happens at the extreme kinematic limit $x \to 1$, where nearly all of the nucleon momentum is carried by a single quark. This limit is dominated by the relative contributions of the u and d valence quarks. Simple phenomenological models like the SU(6) symmetric quark model predict significantly different behavior than perturbative QCD or quark models with improved hyperfine interactions. One can study this region via the ratio of the neutron and proton unpolarized structure functions F_2^n/F_2^p. Although F_2^p is well-known, the tradi-

tional way of extracting F_2^n has been with the use of nuclear targets, which for inclusive experiments requires models for the nuclear physics and a subtraction of the F_2^p background. This leads to large model dependence and systematic uncertainties at high x.

Another interesting question is whether Bloom-Gilman duality holds as well for the neutron as it does for the proton. The beautiful data for F_2^p in the resonance region show remarkable agreement with extrapolations of the deep-inelastic results to lower Q^2 at comparable x, when one averages over the resonance peaks. Although data in the resonance region have been collected in experiment E03-012, corresponding data in the deep-inelastic region are not available. The new data with the 11 GeV beam will allow duality in the neutron structure function to be extensively tested for the first time. Finally, measurements of elastic scattering cross sections on the neutron will give additional information on its form factors at high Q^2, in a largely independent and complementary approach to the existing approved Jefferson Lab experiments.

In this Proposal to the Jefferson Lab Program Advisory Committee, we focus on measurements of the inclusive neutron structure functions at high x, including the resonance and elastic region, with detection of a slow backward–going spectator proton. We concentrate on inclusive scattering of 11 GeV electrons; however, many semi-inclusive and exclusive channels (*e.g.*, pion production) can be studied at the same time with this technique. Future extensions to lower beam energy or other final states are possible.

The proposal extends the 5.3 GeV BoNuS experiment E03-012, which demonstrated the principle of slow proton tagging, taking data on the nearly free neutron structure function up to $x \simeq 0.6$. It will complete the program of large-x measurements of the neutron structure function in the deep-inelastic region.

This proposal had been conditionally approved by PAC30 with the conditions to publish results and to use the recoil detection technique in one more experiment. Two PhD theses have been published [2, 3] and publications of the physics results are under preparation and about to be submitted to the CLAS collaboration for internal review. The eg6 experiments [4, 5] used an almost identical RTPC to detect back-scattered helium nuclei successfully in the Fall of 2009.

In the following, we explain the theoretical motivation and experimental method in more detail. We then describe the target–detector system with a first look at some results of experiment E03-012 and then show the expected results for the proposed experiment from our simulations. We conclude with a summary and our beam time request to the PAC.

3 Physics Motivation and Theoretical Background

Most of our information on the structure of the nucleon — from its elastic form factors, to its deep inelastic structure functions — comes from many decades of experiments on proton targets. A complete determination of the valence content of the nucleon can be achieved only when both its u and d quark distributions are known. This requires charged lepton scattering from the neutron. In principle, the valence u and d quark distributions can be separated via neutrino and antineutrino scattering on the proton. However, to date there have been no measurements performed with the requisite precision to adequately constrain the d quark distribution at large x.

The absence of free neutron targets has meant that the traditional method for extracting neutron structure information has been to use deuterium targets, and apply nuclear corrections arising from the Fermi motion and binding of the nucleons in the deuteron. While this is sufficient in some cases, for many neutron observables, especially ones sensitive to the high momentum components of the deuteron wave function, the nuclear model uncertainties can be rather large. As a result, our knowledge of the structure of the neutron, especially in the deep inelastic region at large x, is inadequate. Given the extremely high quality of proton data that are being accumulated at Jefferson Lab and other facilities, obtaining a similar level of accuracy for the structure of the free neutron is a high priority.

In this section we highlight several examples which would benefit dramatically from a more accurate determination of the structure of the free neutron. We focus on the ratio of d to u quark distributions at large x, which currently has very large (over $\sim 50-100\%$, depending on the nuclear corrections models used) uncertainties for $x > 0.6$. Other quantities which will be able to be measured with the proposed setup include the elastic neutron form factor, quark-hadron duality, large-x parton distribution functions, semi-inclusive DIS channels, hard exclusive reactions such as deeply-virtual Compton scattering or deeply-virtual meson-production, as well as the inclusive structure function of a virtual pion.

Finally, we note that the data could provide an important testing ground for calculations of various nuclear effects in the deuteron. In addition to isolating the kinematics of the recoil proton where these effects are small, the data will also provide coverage into kinematic regions where particular effects, such as dynamical off-shell effects, are expected to become significant.

3.1 Nucleon Structure at Large x

Although a large body of deep inelastic structure function data exists over a wide range of x and Q^2, the region $x > 0.6$ is not well explored. For $x \geq 0.4$ the contributions from the $q\bar{q}$ sea are negligible, and the structure functions are dominated by the valence quarks.

Knowledge of the valence quark distributions of the nucleon at large x is vital for several reasons. The simplest SU(6) symmetric quark model predicts that the ratio of d to u quark distributions in the proton is 1/2; however, the breaking of this symmetry in nature results in a much smaller ratio. Various mechanisms have been invoked to explain why the $d(x)$ distribution is softer than $u(x)$. If the interaction between quarks that are spectators to the deep inelastic collision is dominated by one-gluon exchange, for instance, the d quark distribution will be suppressed, and the d/u ratio will tend to zero in the limit $x \to 1$ [6]. This assumption has been built into most global analyses of parton distribution functions [7], and has never been tested independently.

On the other hand, if the dominant reaction mechanism involves deep inelastic scattering from a quark with the same spin orientation as the nucleon, as predicted by perturbative QCD counting rules, then the effect is to perturb the spin-flavor symmetric wave function such that d/u tends to $\approx 1/5$ as $x \to 1$ [8]. Determining d/u experimentally would therefore lead to important insights into the mechanisms responsible for spin-flavor symmetry breaking.

Because of the 4:1 weighting of the squared quark charges between the up and down quarks, data on the proton structure function, F_2^p, provide strong constraints on the u quark

distribution at large x,

$$F_2^p(x) \;=\; x\sum_q e_q^2\,(q(x)+\bar{q}(x)) \;\approx\; x\left(\frac{4}{9}u(x)+\frac{1}{9}d(x)\right)\;. \tag{1}$$

Note that for simplicity F_2^p in Eq. (1) is written to leading order in α_s; in practice next-to-leading order (NLO) expressions for structure functions are used. The determination of the d quark distribution, on the other hand, requires in addition the measurement of the neutron structure function, F_2^n. In particular, the d/u ratio can be determined (at leading order in α_s) from the ratio of neutron to proton structure functions,

$$\frac{F_2^n}{F_2^p} \;\approx\; \frac{1+4d/u}{4+d/u}\;, \tag{2}$$

provided $x \geq 0.4$ (at a moderate to high Q^2) so that the sea quark content can be neglected. These kinematics are ideal for measurements at Jefferson Lab with an 11 GeV electron beam energy.

In the past, data on F_2^n have been extracted primarily from inclusive scattering off deuterium. Unfortunately, theoretical uncertainties in the treatment of nuclear corrections have led to ambiguities in the extracted F_2^n at large x. In particular, inclusion of Fermi motion and nucleon off-shell corrections in the deuteron can lead to values for F_2^n/F_2^p which differ by 50% already at $x = 0.75$, and by a factor 2–3 at $x = 0.85$ [9, 10, 11, 12]. This uncertainty is illustrated in Fig. 1, which shows F_2^n/F_2^p extracted from the same SLAC data on the proton and deuteron structure functions [9], with the nuclear corrections estimated on the basis of Fermi motion only (squares), taking nucleon off-shell effects into account [10, 12] (diamonds), and using a model assuming suppression of point-like configurations (PLC) in the bound nucleon [12] (triangles). The nuclear model dependence is as large or larger than the spread in the model predictions for the $x \to 1$ behavior, which are indicated by the arrows. The tagged structure function method for measuring F_2^n proposed here virtually eliminates the uncertainties from nuclear models.

3.2 Quark-Hadron Duality for the Neutron

Measurements at Jefferson Lab of the unpolarized structure functions on hydrogen, deuterium and heavier nuclei in the resonance region [13, 14] have established to high accuracy the remarkable phenomenon of Bloom-Gilman duality down to $Q^2 \sim 1$ (GeV/c)^2 or even lower. Also, HERMES has observed duality in the proton spin asymmetry A_1 [15], and JLab data have been analyzed to test duality in the spin-dependent proton and ^{3}He g_1 structure functions. The recently approved MINERvA experiment at Fermilab will investigate duality in neutrino scattering as well.

Quark-hadron duality here refers to the observation that the structure functions in the resonance region at low W and Q^2 show a striking similarity, when averaged over resonances, to the scaling structure functions measured in the deep inelastic region at high W and Q^2. This phenomenon is even more remarkable given that the resonance–scaling duality appears to hold in each of the prominent resonance regions separately, indicating the presence of duality on a rather local level. Although a global version of duality, with integration over

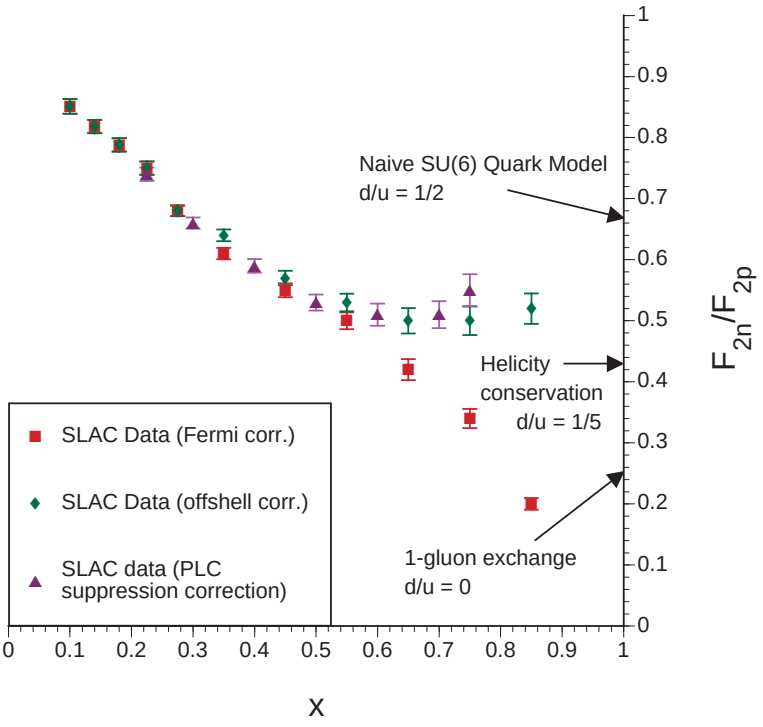

Figure 1: Neutron to proton structure function ratio, extracted from SLAC proton and deuteron data [9], assuming different prescriptions for the nuclear corrections, as described in the text. Several theoretical predictions for the $x \to 1$ limits are indicated by arrows.

many resonances, can be qualitatively understood in the context of the twist expansion in QCD, at present the origin of local duality is unclear and the subject of considerable theoretical interest [16, 17, 18].

The appearance of duality in QCD is usually taken to indicate that the size of higher twist contributions to structure functions, involving long-range correlations between quarks and gluons, is small [19]. As discussed by Close and Isgur [17], the higher twist effects are responsible for the difference between the scaling structure function expressed in terms of an incoherent sum of the squares of quark charges,

$$F_2(x) \;=\; x \sum_q e_q^2 \; q(x) \;, \tag{3}$$

and that given in terms of squares of form factors,

$$F_1 \;=\; M^2 \left(|G_+|^2 + |G_-|^2 \right) \delta(W^2 - M_{N^*}^2) \qquad \text{and} \tag{4}$$

$$F_2 \;=\; (1 + \nu^2/Q^2)^{-1} M\nu \left(|G_+|^2 + 2|G_0|^2 + |G_-|^2 \right) \delta(W^2 - M_{N^*}^2) \;, \tag{5}$$

involving a coherent sum over individual quark flavors,

$$|G_m|^2 \;=\; \left| \sum_q e_q \; G_m^{(q)} \right|^2 \;. \tag{6}$$

Here the helicity amplitudes $G_m(m = \pm 1, 0)$ are defined in terms of $N \to N^*$ transition matrix elements:

$$G_m \quad \propto \quad \langle N^*, \lambda' = m - 1/2 | \epsilon_m^\mu \cdot j_\mu(0) | N, \lambda = 1/2 \rangle \ , \tag{7}$$

with λ (λ') the helicity of the initial (final) state, ϵ_m^μ the photon polarization vector, and j_μ the electromagnetic current. In the flavor-symmetric limit, the difference between these dual descriptions, which represents violations of Bloom-Gilman duality, is precisely due to the presence of higher twist effects. Diagrammatically these can be represented as off-diagonal quark transitions, in which the photon scatters from the nucleon with strength proportional to $\sum_{q \neq q'} e_q e_{q'}$. The experimental verification of Bloom-Gilman duality for the proton [20] implies that the single-quark scattering mechanism dominates the interaction above $Q^2 \sim 0.5$ (GeV/c)^2.

On the other hand, it has been observed that for the specific case of the proton, the sum over the off-diagonal contributions $\sum_{q \neq q'} e_q^{(p)} e_{q'}^{(p)} = 0$ simply because of the quark charge assignments in the proton [17]. This leaves open the possibility that duality for the proton may not necessarily be an indication of suppression of higher twist effects, but merely the result of a fortuitous cancellation of their coefficients. For the neutron, however, there is no such cancellation, since $\sum_{q \neq q'} e_q^{(n)} e_{q'}^{(n)} \neq 0$. Furthermore, within a simple harmonic oscillator quark model, Close and Isgur [17] find that the neutron structure functions should exhibit systematic deviations from local duality, and that duality should occur at higher W for the neutron than for the proton. These arguments can be further refined by considering more sophisticated quark models, including various mechanisms of SU(6) symmetry breaking [21]. The true origins of Bloom-Gilman duality in the nucleon can be determined with the verification of this phenomenon in the neutron.

In the earlier BoNuS experiment at 5.3 GeV, the structure function of the neutron was measured in the nucleon resonance region, at $W < 2$ GeV, over a range of x and Q^2. To test duality, one requires data at the same x but at higher Q^2, in the deep-inelastic region, $W > 2$ GeV. This experiment will therefore provide the vital missing information which will enable the workings of duality for the neutron to be tested directly for the first time at the same level as for the proton.

Very recently a new study [22] of inclusive proton and deuterium data from SLAC and Jefferson Lab has attempted to verify duality in the neutron by extracting F_2^n from the F_2^p and F_2^d structure functions in the resonance region. The findings suggest that duality may indeed be valid to a high accuracy in the neutron, especially in the second and third resonance regions. However, since the neutron data were extracted using a particular model for the nuclear effects in deuterium, it is important to verify these results with direct measurements of F_2^n, and the BoNuS data will be ideal for this purpose.

3.3 Large-x Parton Distribution Functions

Parton distribution functions (PDFs) give the probability to find partons in a hadron as a function of the fraction x of the nucleon's momentum carried by the parton. The nucleon's PDFs are usually determined in global fits to a wide range of cross sections and other observables measured in hard scattering processes capable of resolving the nucleon's short-distance structure. Precise knowledge of the nucleon's flavor structure and precision tests of

the evolution of the leading twist parton densities as predicted by QCD are key questions of present day studies of structure functions. However, such flavor decomposition requires (a) a separation of the flavor nonsinglet and singlet evolution, and (b) precision knowledge of the u and d PDFs over the entire x-range.

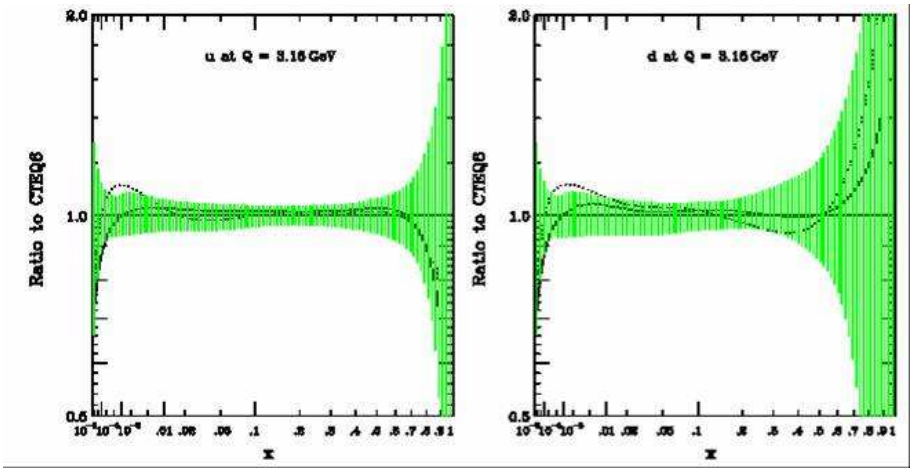

Figure 2: Uncertainty bands for the u and d quark distribution functions at $Q^2 = 10\ \mathrm{GeV}^2/c^2$. The solid line is CTEQ5M1 and the dotted is MRST2001.

Although the PDFs are generally well determined in the small and medium x ranges, their uncertainty grows rapidly for $x > 0.1$. At large x the PDFs are not well determined, as Fig. 2 illustrates for the u and d distributions, with uncertainties rising rapidly as $x \to 1$. The d quark PDF in particular has substantial uncertainty above $x \sim 0.5$, due largely to the lack of available data, and the uncertainties associated with neutron data extrapolated from deuteron measurements.

Very recently, a new global PDF analysis was performed [23] which explored the possibility of further reducing the uncertainties at large x by relaxing the constraints on the kinematics over which data are included in the fit. This fit (referred to as "CTEQ6X") allowed for a significant increase in the large-x data set by including data at smaller W^2 and Q^2 than the standard global fits (such as CTEQ [24] or MSTW [25]) usually allow, and systematically studying the inclusion of target mass and higher twist contributions. In addition to the proton, data on deuterium were also included to better constrain the d-quark distribution, which required the inclusion of nuclear corrections into the fit. While it was observed that this fit led to a stronger supression of the d-quark PDF relative to the CTEQ6 results, it was also noted that the magnitude was very sensitive to the treatment of the nuclear corrections and to the allowed parametrization of the PDFs for $x \to 1$.

Results from the CTEQ6X fit are shown in Figure 3, where the ratio of the PDFs for CTEQ6X and CTEQ6 for both the u-quark (top panel) and the d-quark (bottom panel) are displayed. Although the uncertainties on the PDFs are reduced, the authors note that "... further progress in the determination of the behavior of the large-x PDFs and the d/u ratio requires either a better understanding of the nuclear corrections or the use of data obtained using free nucleons in the initial state, for which we have reviewed several experimental possibilities." We stress, though, that the error bands in Fig. 3 do *not* include uncertainties

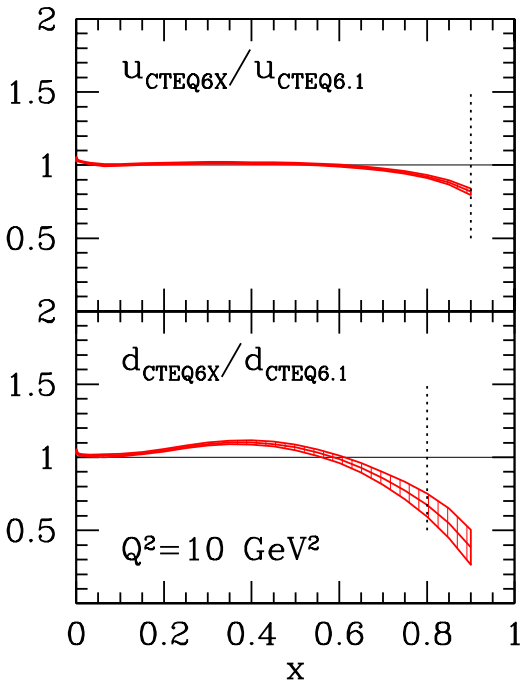

Figure 3: Ratio of CTEQ6X to CTEQ6 results for u and d-quark distribution functions.

arising from the model dependence of the nuclear effects in the deuteron, which is significant above $x \sim 0.7$. The proposed BoNuS neutron structure function measurements at large x will play a crucial role in reducing the uncertainty bands in global PDF fitting efforts.

We mention, additionally, that reliable knowledge of parton distributions at large x is crucial to many searches for new physics signals beyond the standard model in the next generation of collider experiments [26].

3.4 Elastic Electron–Neutron Scattering

The elastic form factors of the nucleon are the most basic observables which reflect its composite nature. As with the DIS structure functions, a considerable body of data now exists on the elastic electric and magnetic form factors of the proton, while the analogous form factors of the neutron are known much less accurately and over a more limited range of kinematics.

The magnetic form factor of the proton is reasonably well determined to $Q^2 = 30\ (\mathrm{GeV}/c)^2$. Accurate measurements of the neutron magnetic form factor, $G_M^n(Q^2)$, currently extend to $Q^2 \approx 5\ (\mathrm{GeV}/c)^2$ (E94-017 [27, 28]), with plans to measure $G_M^n(Q^2)$ to $Q^2 \approx 14\ (\mathrm{GeV}/c)^2$ with the upgraded CLAS12 detector at a 12 GeV CEBAF [27]. These experiments involve quasi-elastic scattering from the deuteron, with measurement of the ratio of scattered neutron to proton events to determine G_M^n/G_M^p. Unfortunately, quasi-elastic measurements at high Q^2 require more elaborate treatments of nuclear corrections, including the effects of

relativity, final state interactions, and possible non-nucleonic degrees of freedom.

The recent experiments at MAMI, Bates and Jefferson Lab measuring double spin observables in quasi-elastic scattering off deuteron and ^{3}He targets allow a nearly model-independent extraction of the ratio G_E^n/G_M^n, up to Q^2 of about 1.5 $(\mathrm{GeV}/c)^2$. In future experiments, this method will be extended to even higher Q^2. However, to extract absolute values of either G_E^n or G_M^n one needs to measure cross sections. The availability of a nearly free neutron target for cross section measurements will enable one to measure different combinations of G_E^n and G_M^n at unprecedented high Q^2, essentially free from uncertainties from nuclear effects as well as neutron detection efficiencies.

Our proposed experiment therefore offers an independent check of other G_M^n measurements with different systematic effects.

3.5 Other Physics Topics Accessible with BoNuS

The following additional physics topics are also of high current interest, and will become accessible with the same recoil detection technology used for BoNuS. At present, however, not all of the necessary equipment or calculations are in hand, so a full exposition will have to await separate dedicated proposals.

3.5.1 Semi-Inclusive Meson Production

Production of mesons in the current fragmentation region of semi-inclusive deep-inelastic scattering from nucleons is an important method of isolating different flavors of partons. Detecting positively or negatively charged pions, for instance, off the proton at large x and large $z = E_\pi/\nu$ preferentially selects u and d quarks, respectively. While semi-inclusive DIS data are rapidly accumulating in electron scattering from protons, no semi-inclusive data exist for neutron targets.

A natural extension of the BoNuS technique in inclusive DIS off the neutron is to consider *semi-inclusive* DIS from a nearly-free neutron in the deuteron. Availability of semi-inclusive neutron data will greatly complement our ability to perform flavor separation of parton distribution functions. In addition to pions, observation of a K^+ as the leading meson produced in the current fragmentation region would imply scattering from either a u or $\bar{s}$ quark. Since isospin symmetry implies that $\bar{s}^p = \bar{s}^n$ (and $u^p = d^n$), by detecting K^+ mesons off the proton and the neutron, one would be sensitive to the u, d, and s quark distribution in the proton, respectively. Other examples inlcude access to flavor asymmetries of the proton sea, $\bar{d} - \bar{u}$, as well as possible tests of charge symmetry breaking in parton distributions.

3.5.2 Pion Cloud of the Nucleon

In the early 1970s, Sullivan [29] pointed out that electron DIS off a proton target includes a contribution originating from scattering off the pion cloud of the nucleon, as shown in Fig. 4. This so-called Sullivan process was shown to persist even at large Q^2 scales. An immediate consequence of the Sullivan process is that the nucleon parton distributions contain a component which can be attributed to the meson cloud. In the early 1980s, Thomas [30] predicted several implications of the Sullivan process for nucleon parton distributions, such

as that the nucleon sea should have a light flavor $\bar{d} - \bar{u}$ asymmetry, as well as a strange $s - \bar{s}$ asymmetry. Support for a $\bar{d} - \bar{u}$ flavor asymmetry was initially provided in the early

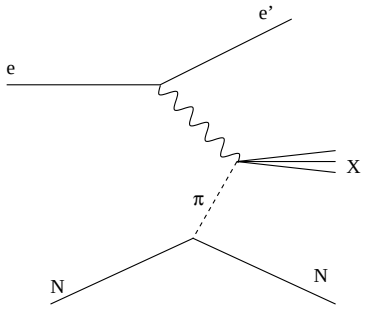

Figure 4: The Sullivan process.

1990's by the New Muon Collaboration's measurement [31] of the violation of the Gottfried sum rule [32]. Independent confirmation of the $\bar{d}/\bar{u}$ flavor asymmetry was later provided by Drell-Yan experiments [33, 34, 35, 36] and the semi-inclusive DIS measurements at HERMES [37].

The success of the meson-cloud model in explaining the $\bar{d}, \bar{u}$ asymmetry suggests that a direct measurement of the meson cloud in DIS should be feasible. At the HERA $e-p$ collider, meson structure functions were measured in a hard diffractive process, where forward-going neutrons or protons were tagged in coincidence with the DIS events [38].

Measurements of meson structure functions could be done with the BoNuS target and detector system using the reactions $p(e, e'p)X$ and $d(e, e'pp)X$. These processes could also contribute a background to the $d(e, e'p)X$ measurement of the neutron structure function in BoNuS, if the detected proton was the result of the Sullivan process instead of being the spectator.

To make measurements of the pion structure function using the Sullivan process to provide a pion target in the semi-inclusive reaction $d(e, e'pp)X$, the spectator proton would be detected in the BoNuS recoil detector and the proton resulting from the pion exchange might be detected in the BoNuS detector or in the CLAS12 detector. Preliminary simulations indicate that the protons resulting from pion exchange are dominantly forward-going and have somewhat higher momenta than the spectators.

Measurements of the semi-inclusive reactions $p(e, e'p)X$ and $d(e, e'pp)X$ in BoNuS were introduced in a Letter of Intent submitted to PAC27 [39], which called for a maximum beam energy of 6 GeV. The reviewers expressed concern that at 6 GeV it is not possible for both M_X to be large and $t_{\min}$ to be small, with t the difference between the initial and final four-momentum of the electron. There was also concern that the measurement would be unable to relate to the pion structure function without duality arguments, or that the measurement would be too far from the pion pole for acceptable extrapolation. Further simulation is required to evaluate the feasibility of the measurement with a beam energy of 11 GeV.

Measurements at Jefferson Lab could be a nice complement to those already taken at HERA. The lower beam energy allows access to a higher x region in the pion structure functions at JLab compared to HERA. The large angular and kinematic coverage for the recoiling proton (or proton pair) using the CLAS12 and BoNuS detectors would allow a detailed study of the Sullivan process as a function of variables including the recoiling proton

momentum and angles. Also, the CLAS12 and BoNuS detectors could allow a detection of the $\Lambda \rightarrow p\pi^-$ decay, making a measurement of the $p \rightarrow K^+\Lambda$ kaon cloud in the nucleon potentially feasible. This could lead to a measurement of kaon structure functions.

3.5.3 Semi-inclusive DIS from $A = 3$ Nuclei

It has been suggested that the ratio of the mirror nuclei ^{3}He and ^{3}H may be measured to precisely obtain the neutron/proton cross section ratio at large x [40]. The BoNuS target could be filled with these gases, and a simple inclusive measurement of this ratio would take substantially less time in CLAS than the direct neutron measurement experiment here proposed, since no spectator tagging would be required. Moreover, for reduced theoretical uncertainty, spectator deuterons from the neutron and proton targets in the mirror nuclei could be measured in the BoNuS RTPC detector just as the protons are currently. This experiment would have differing theoretical uncertainties, and would provide a nice complement to the BoNuS result. However, issues associated with a ^{3}H target still need to be investigated. Measuring the $^3\mathrm{He}(e, e'd)X$ with a spectator d would also allow us to study the spectator mechanism in great detail, since the structure functions of the proton are well known.

3.5.4 Deeply-Virtual Compton Scattering

The discovery of Generalized Parton Distributions (GPD) has opened up a completely new way of mapping out simultaneously the space and momentum components of quarks and gluons inside nucleons, which can be achieved through the process of Deeply Virtual Compton Scattering (DVCS). At JLAB there are four GPDs accessible: $H(x,\xi,t), \tilde{H}(x,\xi,t), E(x,\xi,t)$ and $\tilde{E}(x,\xi,t)$, where the forward limit of $H(x,\xi,t)$ and $E(x,\xi,t)$ are directly related to the quark angular momentum through Ji's sum rule:

$$J_q = \frac{1}{2}\int_{-1}^{1} x[H_q(x,\xi,0) + E_q(x,\xi,0)]dx.$$

Experimentally, DVCS on the proton is measured via the high energy $ep \rightarrow ep\gamma$ reaction and will provide access to two of the four generalized parton distributions $(H, \tilde{H})$ of the nucleon. However, in order to determine the quark angular momentum, also the other GPDs have to be measured. To access the least known and least constrained E, one needs to measure DVCS on the neutron with a polarized beam, using a deuterium target. In such a configuration the contributions from $(H, \tilde{H})$ are suppressed and E is the dominant part. Instead of detecting the neutron in coincidence with the electron, one can measure the recoil proton energy with the BoNuS detector. At low momentum, recoil protons are spectators, and therefore select the quasi-free process on the neutron, thus allowing us to measure the neutron DVCS without detecting the neutron. Depending on the total "effective" luminosity achievable, this may be the preferred method, but final conlcusions will have to await a fully developed proposal.

In addition, the BoNuS RTPC can also be used to detect the recoil nucleus in nuclear DVCS $A(e, e'A\gamma)$, as has already been pioneered with the eg6 experiment [5].

3.5.5 Other Measurement Opportunities

Several Letters of Intent have been submitted to PAC 35 using CLAS12 and the RTPC recoil detector for measurements of nuclear exclusive and semi-inclusive physics and the EMC effect in DIS scattering of light nuclei [41, 42]. These letters of intent have been recommended by the PAC for development into a common full proposal.

4 Tagged Structure Functions

4.1 Spectator Tagging

The measurement of tagged structure functions in semi-inclusive deep inelastic scattering from the deuteron with a slow recoil proton detected in the backward hemisphere will allow the resolution of the ambiguities introduced by nuclear model dependence for deep-inelastic, as well as (quasi-)elastic, scattering [43, 44, 45]. Within the nuclear impulse approximation, in which the inelastic scattering takes place incoherently from individual nucleons, the differential semi-inclusive cross section can be written as a product of the deuteron spectral function, $\mathcal{S}$, and an effective (bound) neutron structure function, $F_2^{n(eff)}$ [45]:

$$\frac{d\sigma}{dx dW^2 d\alpha d^2p_T} \approx \frac{2\alpha_{em}^2(1-\nu/E)}{Q^4}\ \alpha\ \mathcal{S}(\alpha, p_T)\ F_2^{n(eff)}(W^2, p^2, Q^2)\ . \tag{8}$$

(For the full expression for the differential cross section in terms of the transverse and longitudinal structure functions see Ref. [45].) Here $W^2 = (p_d + q - p_s)^2$ is the invariant mass squared of the unobserved hadronic final state, with p_s the momentum of the spectator proton, p_d the momentum of the initial state deuteron, and $p = p_d - p_s$ the momentum of the struck neutron. The variable $\alpha = (E_s - p_s^z)/M$ is the light-cone momentum fraction carried by the spectator proton, and p_T its transverse momentum component (perpendicular to the direction of $\vec{q}$), with $E_s = \sqrt{M^2 + \vec{p}_s^{\,2}}$ the spectator proton energy, and M its mass. The use of the light-cone variable α emphasizes the kinematical dependence of the structure function at high Q^2, since $F_2^{n(eff)}(W^2, p^2, Q^2) \equiv F_2^{n(eff)}(x/(2-\alpha), p_T, Q^2)$. In addition, as discussed in Section 4.2.3 below, the dependence on α is not strongly affected by final state interactions. The pre-factor α in Eq. (8) is related to the so-called "flux-factor" [46]. The degree to which the struck neutron is off-shell is given by

$$M^2 - p^2 \approx 2\vec{p}_s^{\,2} + 2M|\epsilon|\ , \tag{9}$$

where ϵ is the deuteron binding energy. In the limit $p^2 \to M^2$ (and $\alpha \to 1$), the effective neutron structure function $F_2^{n(eff)}(W^2, Q^2, p^2) \to F_2^n(W^2, Q^2, M^2) \equiv F_2^n(x, Q^2)$, the free neutron structure function. The p^2 dependence of $F_2^{n(eff)}$ depends somewhat on the theoretical assumptions made about the off-shell behavior of the photon–bound nucleon scattering amplitude. To avoid these uncertainties one therefore needs to minimize the degree to which the struck neutron is off-shell, by restricting oneself to small values of the spectator proton momentum, p_s. At the low momenta proposed in this experiment the uncertainty associated with the choice of deuteron wave function (or the spectral function, $\mathcal{S}$) is also expected to be quite small.

The calculation of the kinematic variables for the experiment will be done in a covariant way, taking into account the four-momentum vector of the on-shell spectator proton for the calculation of the electron-neutron scattering. The Bjorken scaling variable for the interacting neutron then becomes

$$x^\star = \frac{Q^2}{2\,p^\mu\,q_\mu} = \frac{Q^2}{2\left(\left(M_d - E_s\right)\nu + \vec{q}\ \cdot\ \vec{p_s}\right)}\ , \tag{10}$$

where $q^\mu = (\nu; \vec{q})$ is the momentum transfer 4-vector, $p^\mu = (M_d - E_s; -\vec{p_s})$ is the momentum 4-vector of the off-shell neutron, and M_d is the mass of the deuterium nucleus. In a covariant description the struck nucleon is on its energy shell, but off its mass shell. The mass of the free nucleon M is therefore replaced by the off-shell mass (or virtuality) of the bound nucleon:

$$M^{\star 2} = p_\mu p^\mu = (M_d - E_s)^2 - \vec{p}_s^{\,2}. \tag{11}$$

The invariant mass squared of the final hadronic state in $d(e, e' p_s)X$ can then also be written as:

$$W^{*2} = (p^\mu + q^\mu)^2 = (M_d - E_s + \nu)^2 - (\vec{q} - \vec{p_s})^2\,. \tag{12}$$

Finally, while the formula for the impulse approximation cross section in Eq. (8) above is valid in the high-Q^2 limit, the corrections to the structure functions from finite-Q^2 terms have recently also been evaluated [47, 48].

4.2 Backgrounds

The choice of backward kinematics for the spectator proton serves to minimize effects from final state interactions, as well as independent target fragmentation, while the restriction to small proton momenta mostly eliminates uncertainties associated with the deuteron wave function and on-shell extrapolation. In this section we consider each of these corrections to the impulse approximation in Eq. (8) explicitly. Corrections to the impulse approximation from the breaking of the factorization in Eq. (8) were analyzed in Ref. [49] for the inclusive deuteron structure function, and found to be quite small ($\leq 1\%$) for the kinematics considered here. The total estimated errors to F_2^n resulting from these corrections are given in Section 6.

4.2.1 Target Fragmentation

The production of low momentum protons originating from the hadronic debris of the struck neutron is minimized by enforcing a large rapidity gap between the recoil proton and the rest of the hadronic debris [44, 50]. While in the forward hemisphere (current fragmentation region) there are potentially large contributions from direct quark→proton fragmentation, especially at low x, in the backward hemisphere (target fragmentation) these will be strongly suppressed. The direct fragmentation contribution is also expected to decrease with decreasing spectator proton momentum.

Non-spectator protons can be produced in coincidence with DIS electrons through several processes, none of which contributes significantly to the spectrum of *backward-moving*

protons. First of all, protons in the current quark fragmentation region will be exceedingly rare in our kinematics (because of the high W needed to produce a baryon-antibaryon pair) and will be going forward with respect to $\vec{q}$. Secondly, protons could come from the target fragmentation when either a neutron or a proton is struck by the virtual photon.

The Sullivan process described earlier can be considered as part of this signal. However, one can prove rigorously that no such proton can be moving backward either in the lab or relative to $\vec{q}$ if the initial struck nucleon was at rest. For instance, a preliminary simulation of the Sullivan process scattering in the BoNuS kinematics indicates that the protons resulting from the two processes, $e\ n \rightarrow e'\ p\ X$ (with $n \rightarrow \pi^-\ p$) and $e\ p \rightarrow e'\ p\ X$ (where $p \rightarrow \pi^0\ p$), should be peaked in the forward scattering direction and at higher momenta than the spectator proton. For protons or neutrons moving initially backwards inside the deuteron target, a target fragment moving backwards in the final state is possible but requires large initial backward momentum, which is highly suppressed by the deuteron wave function.

These features are evident from Fig. 5, where the ratio of the plane wave impulse approximation (PWIA), corrected for target fragmentation, to the pure PWIA contribution is shown as a function of the recoil angle, θ_{pq}, of the proton relative to the photon direction. Clearly, the effects of target fragmentation are relevant only in the forward hemisphere, and for $\theta_{pq} > 90^\circ$ are totally negligible, even for large p_s.

4.2.2 Off-Shell Corrections

To minimize theoretical uncertainties associated with extrapolation of the semi-inclusive cross section to the nucleon pole, it is important that the tagged structure functions be measured for kinematics where the difference $p^2 - M^2$ is as small as possible. To assess the potential model dependence of the extracted neutron structure function on the extrapolation procedure we consider several models based on rather different dynamical assumptions.

In convolution models off-shell corrections appearing at leading twist originate both kinematically, as a consequence of the nucleon's transverse motion in the nucleus, and dynamically, from modifications of the bound nucleon structure. Kinematical off-shell effects can be calculated with very little model dependence, as discussed in Ref. [51], for instance. Dynamical off-shell effects, on the other hand, depend on descriptions of the intrinsic deformation of the bound nucleon structure, and are therefore more model-dependent.

In the covariant spectator model of Ref. [49], the DIS from a bound nucleon is described in terms of relativistic vertex functions which parametrize the nucleon–quark–"diquark" interaction (where "diquark" here refers to a system of a nucleon with one quark removed, which has the quantum numbers of a diquark). The dependence of the vertex functions on the quark momentum and the "diquark" energy is constrained by fitting to the on-shell nucleon (proton) structure function data. The additional dependence of the vertex function on the virtuality of the off-shell neutron is fixed by comparing the calculated deuteron structure function with the inclusive F_2^d data. The resulting ratio $R_n \equiv F_2^{n(eff)}(W^2, Q^2, p^2)/F_2^n(W^2, Q^2)$ of the bound to free neutron structure functions is shown in Fig. 6 as a function of the momentum of the spectator proton, $|\vec{p}_s| = |\vec{p}|$, for several values of x. Not surprisingly, the effect at low $|\vec{p}_s|$ is very small, with the deviation from unity increasing at higher momenta. For $|\vec{p}| \approx 100$ MeV/c the effect is $\leq 1\%$ for $x = 0.6$, where the EMC effect is more pronounced, and essentially zero for $x = 0.3$.

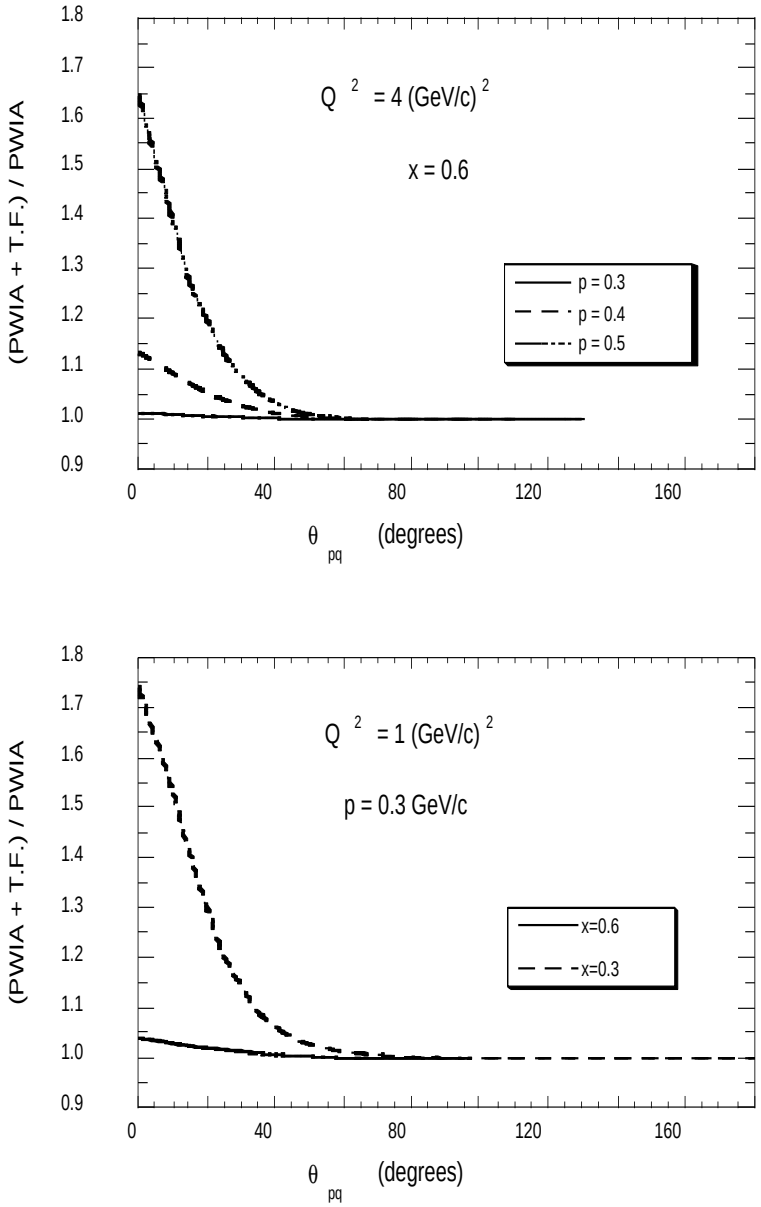

Figure 5: Effect of target fragmentation (TF) on the plane wave impulse approximation (PWIA) calculation of semi-inclusive DIS from the deuteron [44], as a function of the c.m. angle, θ_{pq}, between the spectator proton and the virtual photon.

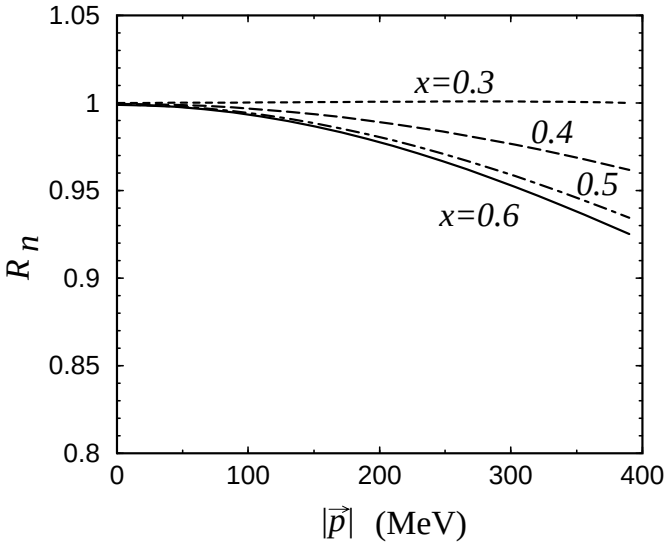

Figure 6: Ratio $R_n \equiv F_2^{n(eff)}(W^2, Q^2, p^2)/F_2^n(W^2, Q^2)$ of the bound to free neutron structure functions, as a function of the spectator proton momentum, in the model of Ref. [49], at $Q^2 = 5$ (GeV/c)^2.

A similar model in which the scattering from an off-shell nucleon is described in terms of a relativistic quark spectral function was introduced in Ref. [51]. In this approach the bound nucleon structure function is evaluated from the free nucleon structure function at a shifted value of the quark light-cone momentum fraction, which depends on the mass of the spectator "diquark" system, the bound nucleon momentum, and the binding energy [51]. The resulting ratio R_n of the bound to free neutron structure functions is shown in Fig. 7.

The deviation from unity is again small at low spectator proton momenta, amounting to $\leq 2\%$ for $|\vec{p}_s| \leq 100$ MeV/c, increasing to around 5% for $|\vec{p}_s| = 200$ MeV/c. The results shown are for $Q^2 = 10$ (GeV/c)^2, although the Q^2 dependence is weak. In contrast to Fig. 6, however, the effect in this model is only weakly dependent on x. Similar behavior to that in Figs. 6 and 7 is also observed in the model of Ref. [52] (see also Ref. [47]), where the assumption of weak binding in the deuteron allows one to calculate the off-shell dependence up to order $\vec{p}^2/M^2$. An important constraint on the size of the nucleon's deformation in this approach is provided by the conservation of the number of valence quarks in the bound nucleon,

$$\frac{d}{dp^2} \int_0^1 dx\, q_{val}^{(eff)}(x, Q^2, p^2) = 0 \ , \tag{13}$$

where $q_{val}^{(eff)}$ is the valence quark distribution in the effective nucleon structure function, $F_2^{N(eff)}$. By imposing this constraint, one obtains an overall reduction of the kinematical off-shell effects whose strength can be located either at intermediate values of x, $x \geq 0.4$, as in the models of Refs. [49, 52], or at low values of $x \leq 0.15$, as suggested in Ref. [53].

Neglecting the contributions of $N\bar{N}$ pairs to the deuteron wave function, another estimate of the role of nucleon off-shellness can be made simply on the basis of kinematics. In the instant form approach discussed in Ref. [54], the nuclear structure function is related to the free nucleon structure function, evaluated at a shifted energy transfer, $\nu \to \bar{\nu}$, which depends

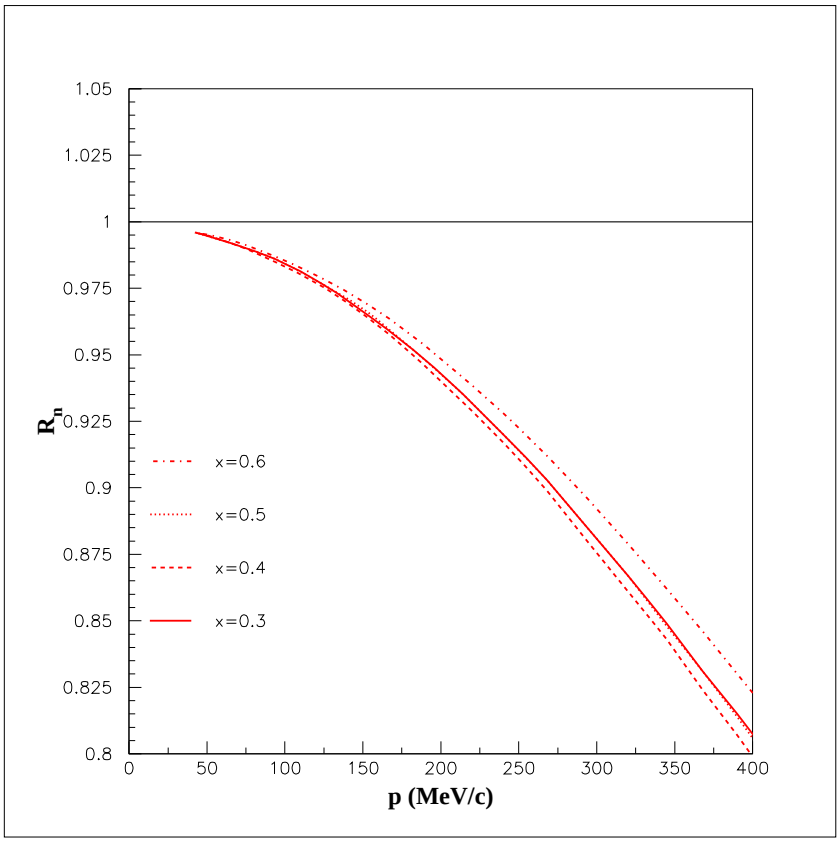

Figure 7: Ratio R_n of the bound to free neutron structure functions, as a function of the spectator proton momentum, in the model of Ref. [51].

on the degree to which the nucleon is bound (and hence, in the instant form language, off its energy shell). A shifted value of ν corresponds to a shifted value of x and Q^2 at which the nucleon structure function is evaluated. The ratio of the structure functions calculated in the plane wave impulse approximation with the modified variables ("PWIA($\bar{q}$)") to that in which there is no modification is displayed in Fig. 8 as a function of θ_{pq} for $Q^2 = 1$ (GeV/c)^2. Once again, one sees that for low spectator proton momenta, $|\vec{p}_s| \approx 100$ MeV/c, the off-shell modification is less than 1% for all accessible angles. Only when one goes above $|\vec{p}_s| \approx 200$ MeV/c are there any effects at the $\leq 5\%$ level.

While the off-shell modification of the bound nucleon structure function in the above models is weak, the color screening model for the suppression of point-like configurations in bound nucleons [12] predicts somewhat larger deviations from unity of the ratio R_n than that in Figs. 6, 7 and 8. In this model one attributes most or all of the EMC effect to a medium modification of the internal structure of the bound nucleon, and little of the effect to mechanisms such as nuclear binding. On the other hand, since the deviation of the bound to free structure function ratio from the free limit is proportional to $2\vec{p}_s^{\,2} + 2M|\epsilon|$ (Eq. (9)), sampling the data as a function of $\vec{p}_s^{\,2}$ should provide some guidance for a smooth extrapolation to the pole. In practice, considering a momentum interval of 70–200 MeV/c will allow the dependence on p^2 to be constrained. Existing 6 GeV data from the JLab experiment E94-102 (E6) will in addition constrain the behavior of the bound structure

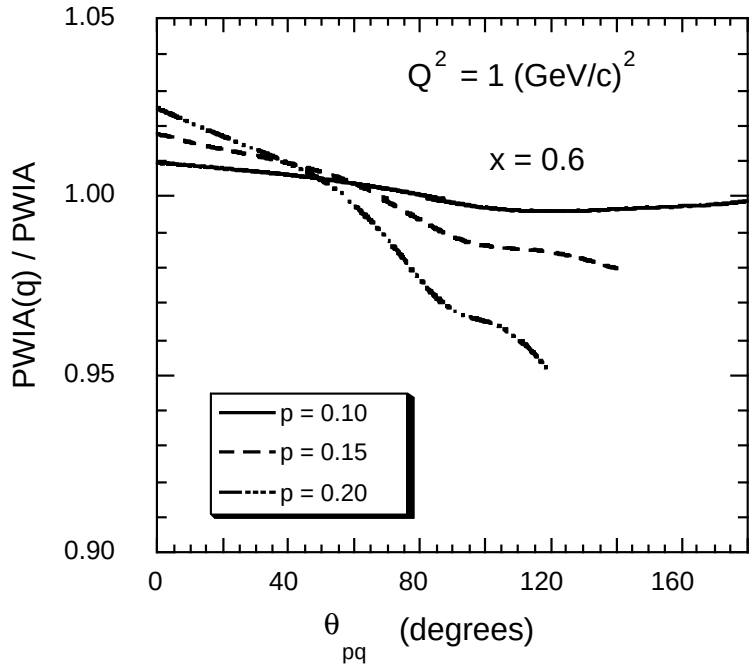

Figure 8: Ratio of bound to free nucleon structure functions, calculated using the model of Ref. [54]. The spectator proton momentum p is in units of GeV/c.

function at larger $|p^2|$ (for spectator momenta between ≈ 250 and 700 MeV/c).

Overall, we expect that the extrapolation from the minimum $|\vec{p}_s| \approx 70$ MeV/c, where the bound neutron is only around 7 MeV/c away from its mass-shell, should be relatively free of ambiguities. This is also supported by recent ^{4}He$(\vec{e}, e'\vec{p})$ polarization transfer experiments at Mainz and Jefferson Lab [55] which indicate that the magnitude of the off-shell deformation may be rather small. These experiments measured the ratio of transverse to longitudinal polarization of the ejected protons, which is related to the medium modification of the electric to magnetic elastic form factor ratio.

Using model-independent relations derived from quark-hadron duality, one can relate the medium modifications in the form factors to a modification at large x of the deep inelastic structure function of the bound nucleon [56], which suggests an effect of $< 3\%$ for $x \leq 0.8$. The typical momentum of the knocked out protons in the experiments was ~ 50 MeV/c, although the results of the analysis were found not to depend strongly on the proton momentum [56]. These considerations lead us to expect that the extrapolation of the bound neutron structure function to the nucleon pole should introduce minimal uncertainty into the extracted structure function of the free neutron – see also Ref. [57].

4.2.3 Final State Interactions

Another possible source of uncertainty arises from final state interaction (FSI) effects, or rescattering of the spectator proton by the deep inelastic remnants, X, of the scattered neutron. The choice of backward angles is designed to minimize these effects. The magnitude of FSI effects has been estimated in several models, within the framework of the distorted

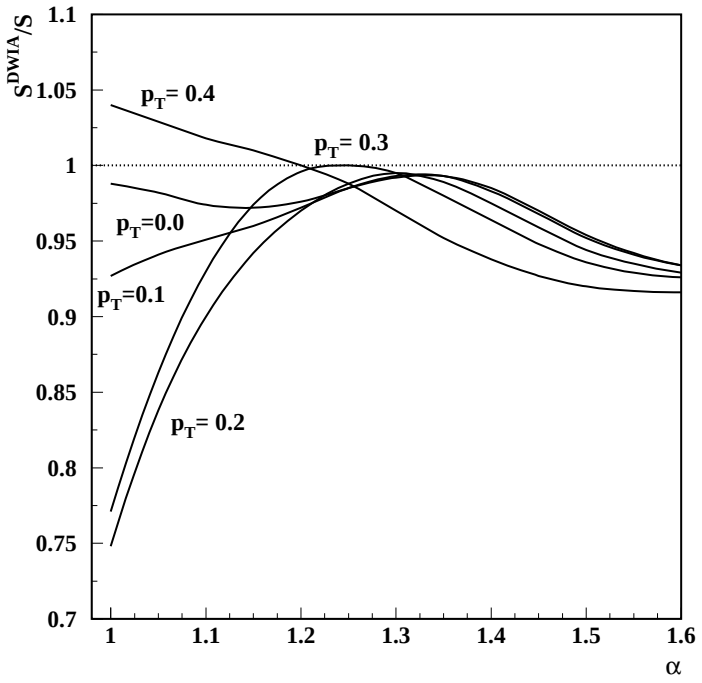

Figure 9: Spectral function calculated with and without FSI effects within the DWIA [45]. The curves correspond to different values of the spectator proton transverse momentum p_T (in GeV/c).

wave impulse approximation (DWIA) [58], and in a string-like model which emphasizes the propagation and hadronization of the partonic debris emanating from the photon–bound nucleon vertex [59]. The strong suppression of FSIs at backward spectator proton angles is evident in both of these calculations.

A direct calculation of the FSI contribution to the cross section requires knowledge of the full dynamics of the spectator proton–X system. In the model of Ref. [58] the effects of FSIs are estimated by comparing with the calculation of FSI effects in the high-energy ^{2}H$(e,e'p)n$ break-up reaction. The effective p–X interaction cross section, σ_{eff}, is approximated [60] by that extracted from soft neutron production in the high-energy DIS of muons from heavy nuclei [61]. The effect of the FSI is then to modify the spectral function $\mathcal{S} \to \mathcal{S}^{DWIA}$ [58], where

$$\mathcal{S}^{DWIA}(\alpha, p_T \approx 0) \sim \mathcal{S}(\alpha, p_T \approx 0) \left[1 - \frac{\sigma_{eff}(Q^2,x)}{8\pi \langle r^2_{pn} \rangle} \frac{|\psi_d(\alpha, \langle p_T \rangle) \psi_d(\alpha, 0)|}{S(\alpha, p_T \approx 0)/\sqrt{E_s \; E_s(\langle p^2_T \rangle)}} \right] , \quad (14)$$

with $\langle r^2_{pn} \rangle$ the average separation of the nucleons within the deuteron, and $E_s(\langle p^2_T \rangle) = \sqrt{M^2 + p_s^{z\;2} + \langle p^2_T \rangle}$ the energy evaluated at the average transverse momentum, $\langle p^2_T \rangle^{1/2} \sim$ 200–300 MeV/c, transferred for the hadronic soft interactions with effective cross section σ_{eff}. The steep momentum dependence of the deuteron wave function, $|\psi_d(\alpha, \langle p_T \rangle)| \ll |\psi_d(\alpha, p_T \approx 0)|$, ensures that FSI effects are suppressed in the extreme backward kinematics.

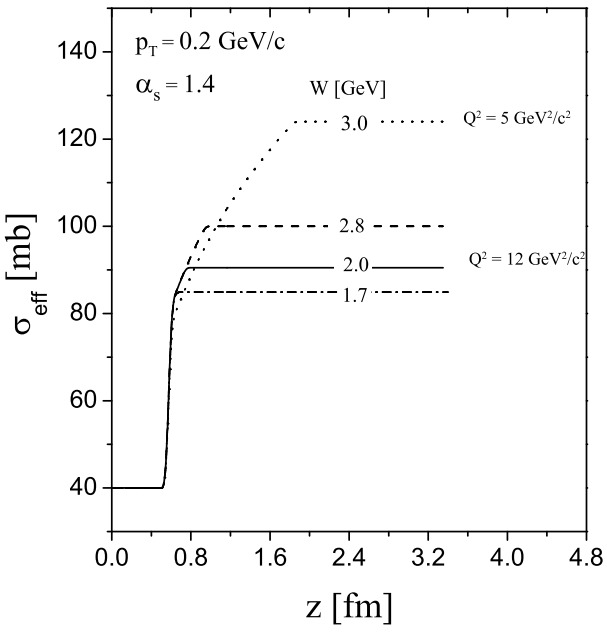

Figure 10: The debris–nucleon effective cross section, σ_{eff}, from Eq. (15) [59], as a function of the longitudinal distance z.

The effects of FSIs in this model are illustrated in Fig.9, which shows the ratio of the light-cone spectral function including FSI effects within the DWIA to that without [45]. At extreme backward kinematics ($p_T \approx 0$) one sees that FSI effects contribute less than $\sim 5\%$ to the overall uncertainty of the $d(e,e'n)X$ cross section for $\alpha \leq 1.5$. For $p_T = 0.1$ GeV/c the FSI effects are minimized at $\alpha = 1.3$, and remain at the $\leq 5\%$ level for values of α ($\alpha = 1.08$) typical in this experiment.

A more microscopic treatment of the effective rescattering cross section was developed recently in Ref. [59]. Here the FSI due to the propagation of the struck nucleon debris and its hadronization in the nuclear environment was applied to the $A(e,e'(A-1))X$ reaction, in which the residual $(A-1)$ nucleus is detected in coincidence with the scattered lepton. For a deuteron target, this process precisely coincides with that considered here, namely ^{2}H$(e,e'N)X$. The effective cross section, σ_{eff}, describing the interaction of the debris with a nucleon of the $(A-1)$ spectator system in this approach is both time- (t) and Q^2-dependent. This result was obtained on the basis of a model [59] which takes into account both the production of hadrons due to the breaking of the color string, which is formed after a quark is knocked out from a bound nucleon, as well as the production of hadrons originating from gluon radiation [62]. The general expression has the form:

$$\sigma_{eff}(t) = \sigma_{tot}^{NN} + \sigma_{tot}^{\pi N}\Big[n_M(t) + n_G(t)\Big] \ , \tag{15}$$

where σ_{tot}^{NN} and $\sigma_{tot}^{\pi N}$ are the total nucleon-nucleon and meson-nucleon scattering cross sec-

tions, and $n_M(t)$ and $n_G(t)$ are the effective numbers of created mesons and radiated gluons, respectively. The dependence of σ_{eff} on t (or equivalently on z, the longitudinal distance) and Q^2 or W is illustrated in Fig. 10.

Once the effective cross section of the interaction of the quark debris with the nucleons is defined, the standard eikonal approximation can be used to evaluate the cross section by replacing the struck nucleon momentum distribution with the distorted momentum distribution [63],

$$S^{PWIA}(\vec{p}_s) \to S^{FSI}(\vec{p}_s) = \frac{1}{3}\frac{1}{(2\pi)3}\sum_{\mathcal{M}_d}\left|\int d\vec{r}\ \Psi_{1,\mathcal{M}_d}(\vec{r})S(\vec{r})\chi_f^\dagger\ \exp(-i\vec{p}_s\cdot\vec{r})\right|^2 , \qquad (16)$$

where the relative coordinate $\vec{r} = \vec{b} + z\vec{q}/|\vec{q}|$ is defined in terms of the longitudinal, z, and perpendicular, $\vec{b}$, components, with the z axis along $\vec{q}$. Here χ_f is the spin wave function of the final state, and $S(\vec{r})$ is the S-matrix describing the final state interaction between the debris and spectator nucleon,

$$S(\vec{r}) = 1 - \theta(z)\,\frac{\sigma_{eff}(z)(1-i\beta)}{4\pi b_0^2}\ \exp(-b^2/2b_0^2)\ , \qquad (17)$$

where β is the ratio of the real to imaginary parts of the scattering amplitude, and the step function $\theta(z)$ arises from the high energy approximation of the Glauber theory. The above equations can also be used to calculate quasi-elastic scattering by replacing the debris-nucleon cross section with the nucleon-nucleon cross section.

The effects of FSIs in this model are illustrated in Fig. 11, where the ratio of spectral functions with and without FSI corrections is shown as a function of θ and $|\vec{p}_s|$. For low spectator momenta, $|\vec{p}_s| \leq 100$ MeV/c, the effects at backward angles ($\theta \geq 130^\circ$) are quite small, $\leq 5\%$. At larger momenta, $|\vec{p}_s| \approx 200$ MeV/c, FSIs introduce some 20–30% enhancement of the spectral function. The effects of FSIs become dominant at perpendicular angles, $\theta \sim 90^\circ$, where for $|\vec{p}_s| = 200$ MeV/c they reduce the ratio of spectral functions by some 75%. Of course, the study of FSI and hadronization effects is interesting in its own right, and can be pursued by focusing on the kinematical region around $\theta \sim 90^\circ$. On the other hand, the results of the model calculations in Figs. 9 and 11 give us confidence that the effects of FSIs at backward angles are at the $\leq 5\%$ level for $|\vec{p}_s| \leq 100$ MeV/c, and will constitute a small correction to the impulse approximation in Eq. (8).

The combined effects of FSIs and nucleon off-shell deformation on the extracted free neutron structure function are illustrated in Fig. 12, where we plot the effective F_2^n at $x = 0.7$ and $Q^2 = 10$ (GeV/c)^2 normalized to the free value as a function of the kinetic energy of the spectator proton, E_{kin}. The dashed and dotted lines represent the color screening [12] and color delocalization [65] models, respectively, and curves with the squares contain FSI effects. The measured tagged neutron structure function is extrapolated to the region of negative values of E_{kin}, in analogy with the Chew–Low procedure for extracting the pion cross section from $p(e,e'\pi)X$ data [66], with the pole of the off-shell neutron propagator in the PWIA amplitude located at $E_{kin}^{pole} = -(|\epsilon_D| - (M_n - M_p))/2$. The virtue of such an extrapolation is that the scattering amplitudes containing final state interactions do not have singularities corresponding to on-shell neutron states. Thus, isolating the singularities through the extrapolation of effective structure functions into the negative spectator kinetic

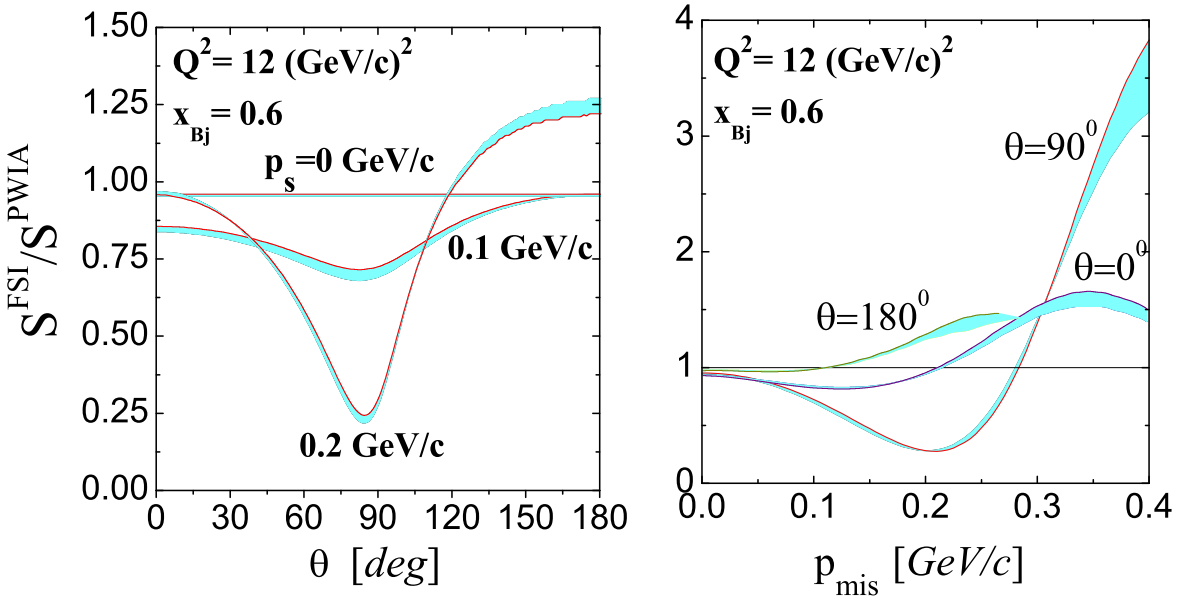

Figure 11: The momentum and angular dependence of the ratio S^{FSI}/S^{PWIA}, at Q^2 = 12 GeV$^2/c^2$ and $x = 0.6$ (updated calculations by the authors of [64]). Left panel: dependence on the angle between the spectator proton and the virtual photon direction. Right panel: dependence on spectator momentum.

energy range will suppress the FSI effects in the extraction of the free F_2^n [57]. For the proposed kinematics, the range of spectator proton momenta would correspond to E_{kin} between 2.5 and 5 MeV. Figure 12 demonstrates that such an extrapolation can be done with the introduction of less than $\sim 4\%$ systematic error.

5 Experimental Setup and Recoil Detector

The first target and recoil detector were built for the BoNuS experiment E03-012 which successfully took data in Hall B in the Fall of 2005 with electron beam energies of 2.1, 4.2, and 5.3 GeV. That experiment covered the kinematical range of the nucleon resonances up to the region of deep-inelastic scattering (DIS). A new detector and target had to be built, which allowed to detect the recoiling low momentum spectator protons at backward angles. Because of the low momenta of the protons, their energy loss is very large and the material in the path of the protons needed to be minimized to avoid too large momentum loss or absorption. Together with the requirement for the angular coverage the detector needed to be close to the target and the target itself of low density to allow the scattered protons to emerge from it. Additionally, an annulus of about 2 cm radius around the beam line needed to be kept as free as possible of materials to avoid interaction of the beam halo and

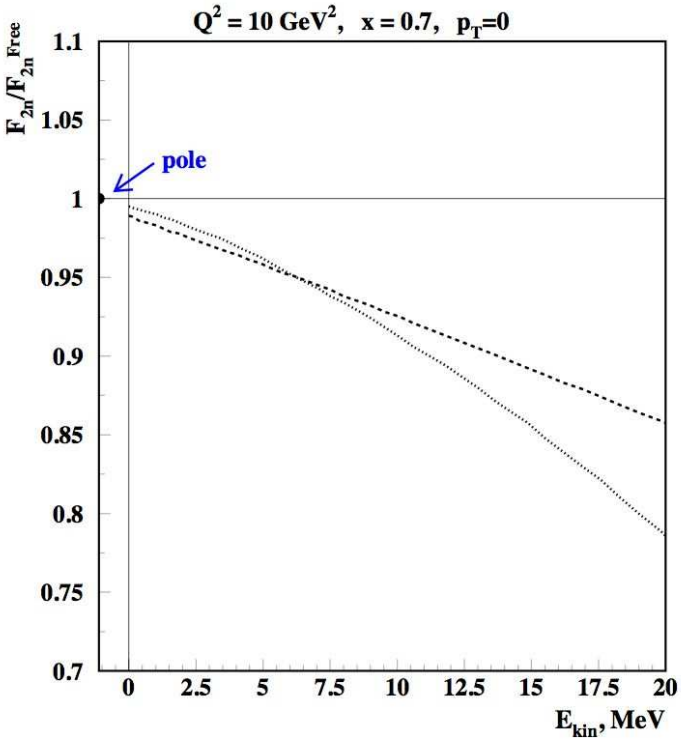

Figure 12: Effect of FSIs on the E_{kin} dependence of the extrapolated neutron structure function, normalized to the on-shell structure function, at extreme backward angles. The dashed and dotted lines represent the color screening [12] and color delocalization [65] models, respectively.

Møller electrons with the target–detector assembly. The assembly had to be installed inside a solenoidal magnetic field to force the Møller electrons into trajectories spiraling in the forward direction and to provide the spectrometer magnetic field for the measurement of the curvature of the scattered protons.

The built apparatus consists of a radial time projection chamber (RTPC), 20 cm long and 14 cm in diameter, surrounding a 23 cm long target tube in its center. The RTPC is described in detail in [67]. The target–detector system was installed inside the 5 Tesla solenoid magnet built for the DVCS experiment (E01-113). For the proposed experiment we are planning to replace the silicon vertex detector inside the central CLAS12 region by a similar target–detector system. This is shown in Figure 13. We would leave the forward vertex detector (FVT) in place. In the present design, carried out at Saclay, it consists of six layers of micromega detectors, covering the scattering angle from 5° to 35°. It is shown in Fig. 14.

The possiblilty to leave the FVT in place when removing the silicon vertex detector is presently being studied. In case it is not, the BoNuS12 collaboration is intending to build a second micromega detector for forward vertex tracking attached to the downstream end of the RTPC. Plenty of space is available inside the bore of the central detector solenoid for the space required by the RTPC plus FVT. The present budget for building the FVT is a

modest $80k.

An overview of the capabilites of the new CLAS12 detector can be found in [68], a document prepared for PAC30.

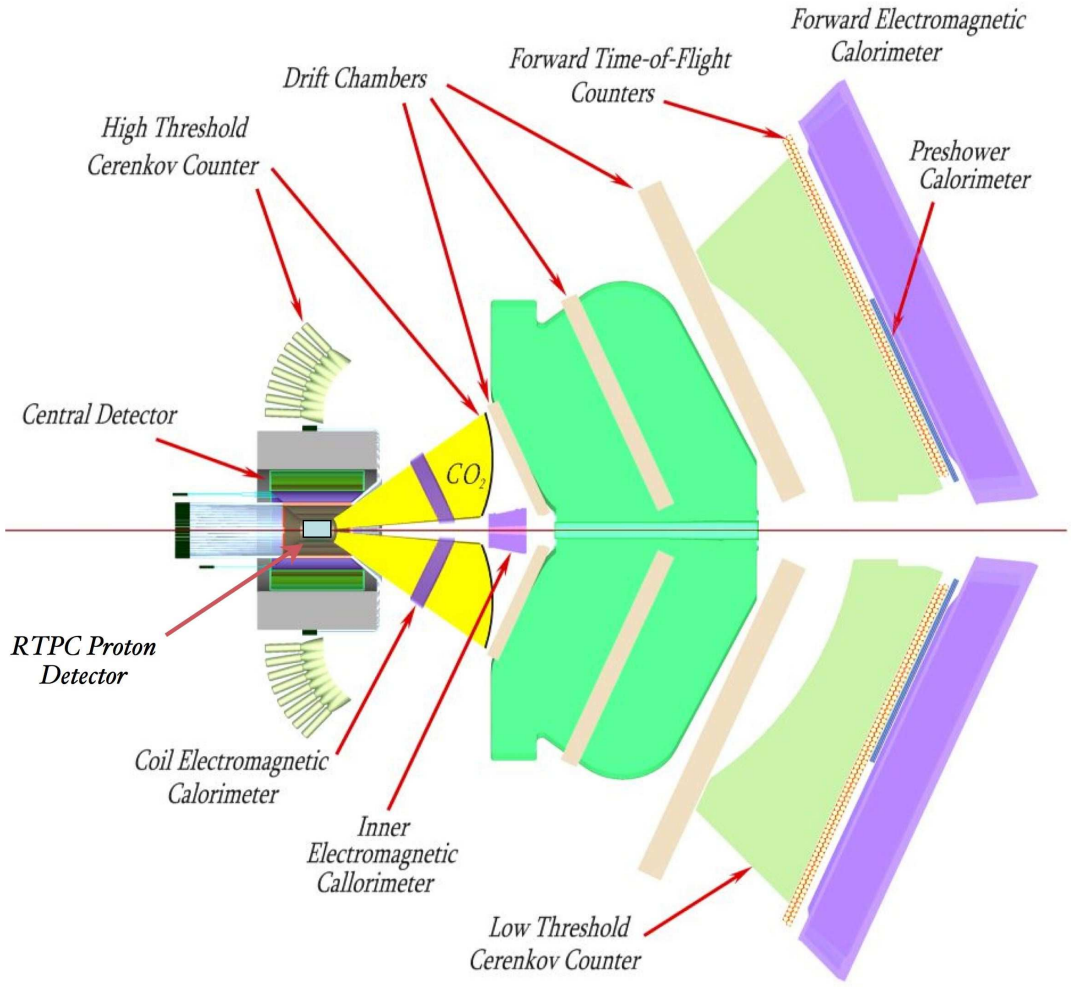

Figure 13: Thin deuterium target and radial TPC for proton detection shown inside the central detector of CLAS12.

5.1 Central Detector Solenoid

Both the target and the spectator proton detector will be located inside the central detector solenoidal magnet. The longitudinal magnetic field from this solenoid will force the Møller electrons into trajectories spiraling into the forward direction and, hence, suppress this background inside the recoil detector. The solenoid will also provide the analyzing magnetic field

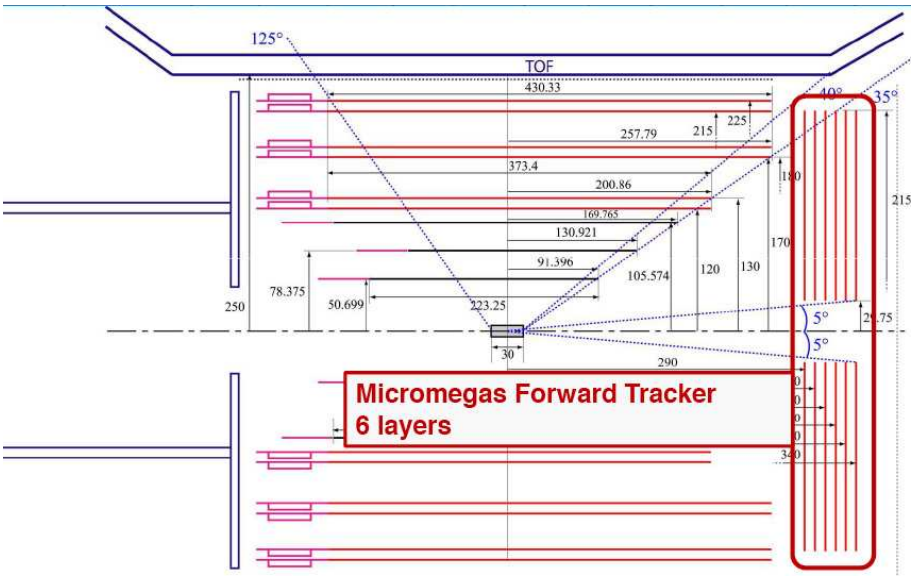

Figure 14: The central detector with silicon vertex tracker (SVT) and forward vertex tracker (FVT), consisiting of six layers of micromega detectors.

for bending the recoil proton tracks inside the RTPC for the momentum measurement.

5.2 Radial Time Projection Chamber

The cylindrical RTPC built for experiment E03-012 had to fulfill several criteria, of which the constraint to fit inside the 220 mm bore of the DVCS solenoid is not required here. The sensitive drift region of the RTPC was an annulus with the inner radius of 30 mm and an outer radius of 60 mm. Materials between the target and the sensitive detector volume had to be minimized to prevent energy loss of the scattered protons and to minimize the interaction of background particles. Background particles are mostly Møller ellectrons forced onto helical trajectories into the forward direction along the beam axis.

The amplification of the drifting electrons was achieved by three layers of Gas Electron Multiplier (GEM, see Ref. [69]) foils at radii of 60, 63, and 66 mm. This was surrounded by a cylindrical readout surface featuring rectangular pads at a radius of 69 mm.

The resulting detector consisted of two similar half-cylinder units which are mated together on either side of the central beam axis. Axial mechanical structures fit within a $\pm 16°$ wedge along the top and bottom of the assembly, as shown in Fig. 15. All of the structural components were machined out of Ultem®. Each subassembly (window, cathode, three GEMs, and padboard) was self-supporting. These parts nest together to form the whole detector module. The interior walls of the drift region (two endcaps and two vertical surfaces forming segments of a chord through the cylinder) are printed-circuit (PC) boards patterned with metal traces forming the field cage. The axial PC boards extended above and below the active portion of the detector and provide the high-voltage divider circuits and connection points, as well as pulse-injection circuitry for testing the electronics.

For the eg6 experiments [4, 5], which took data in the Fall of 2009, a new RTPC and target with some improvements were built. The overall dimensions remained the same,

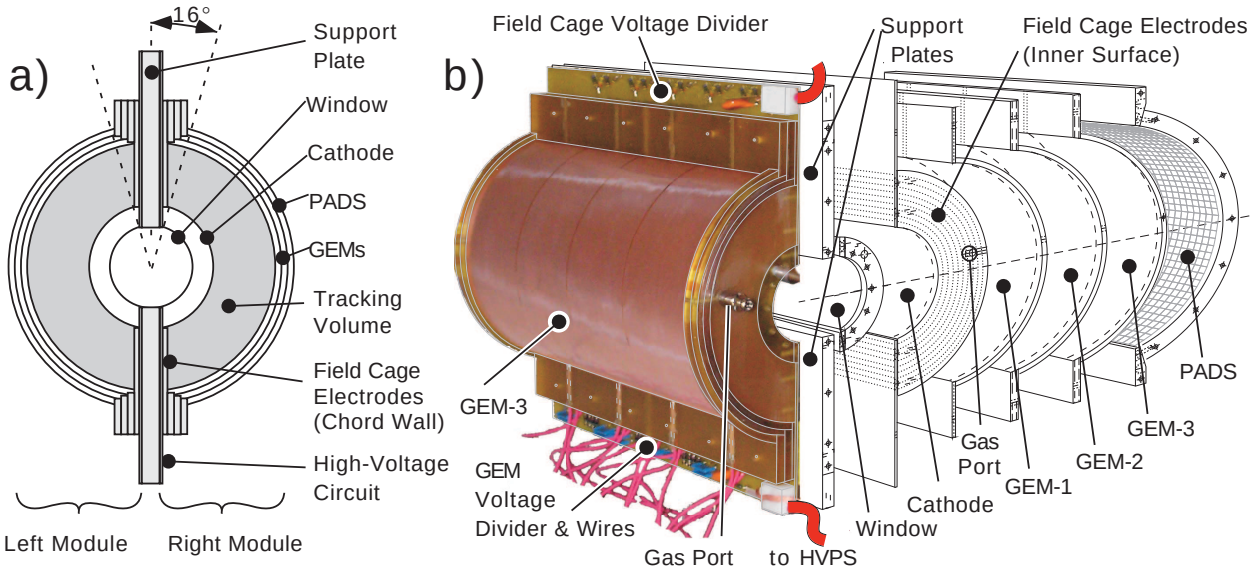

Figure 15: Photograph and Schematic Diagram of the BoNuS RTPC (from [67]). a) Cross-section view through the center of the detector. b) Photograph of the left module with the readout padboard removed and a complementary exploded view exposing the components of the right module.

but the support of the GEM foils and readout plane were redesigned to improve the radial homogeneity of the electric fields insde the RTPC. The structure of two half detectors was replaced by a single detector using fully cylindrical GEM and readout planes. For the GEM foil planes, the originally designed GEM foils were used with two of those glued together to form a cylinder. Due to the changes, the acceptance of the RTPC was increased. This modification induced a change in the structure and building procedure of the detector. Tests and construction of the detector took place during the summer of 2009 and finally the new chamber was used in the eg6 run at the end of 2009. In Fig. 16 the eg6 RTPC is shown during assembly.

For the new BoNuS12 experiment proposed here, we are planning to double the target gas cell length leading to an approximate doubling in luminosity, which will reduce the data taking time, while keeping the event to background ratio constant. Because the relative importance of end planes and target entrance and exit foils is reduced in the longer design, the RTPC acceptance and efficiency will be greatly increased. By using a single GEM foil for a given GEM plane and using the cylindrical arrangement as for the eg6 experiment, the 64° inactive azimuthal region of the BoNuS detector can be reduced to an inactive azimuthal region of 10°. In addition, like in the eg6 experiment, tracks are not disconnected by the half-cylinder support structure. Together with increased azimuthal coverage, the effective tagged rate $d(e,e'p)X$ will increase significantly more than twofold. A longer target gas cell requires the design and construction of a longer RTPC. An increased range of angular backward scattering anlges of the spectator protons will be a very beneficial byproduct. To not loose position (momentum) resolution, the number of readout channels will be similarily doubled.

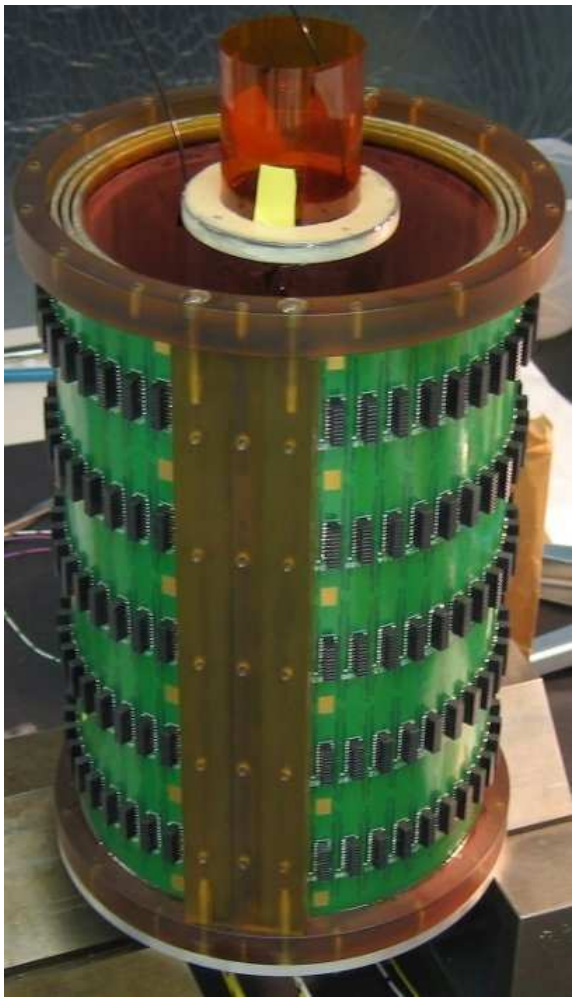

Figure 16: Photograph of the eg6 RTPC during assembly. The 360° continuous GEM and readout planes can be seen at large radii.

To improve the momentum resolution of the spectator protons we studied the effect of increasing the radial drift region from the present 3 cm to 6 cm. The same RTPC simulation as used for the spectator proton acceptance studies was employed and yielded a relative improvement of 50%. With the additional track length inside the RTPC, the track curvature of higher momentum spectator protons will be more pronounced and enable us to extend our momentum range to higher values as well. Given this result, we are planning to increase the RTPC drift region radially.

The investment into the new RTPC and additional readout channels will be modest and could be financed by outside grants to be obtained by university groups involved with the experiment.

5.3 Drift Gas

The RTPC is filled with an ionizable gas. During the BoNuS experiment a mixture of 80% helium and 20% dimethyl ether (DME) was used. To improve the energy loss dE/dx

resolution inside the drift gas for the eg6 experiment, where recoiling helium nuclei had to be detected, the RTPC gas mixture was changed to 80% neon and 20% DME.

A comparison of energy loss as a function of momentum for alpha particles for the two gas mixtures from a simulation is shown in Fig. 17.

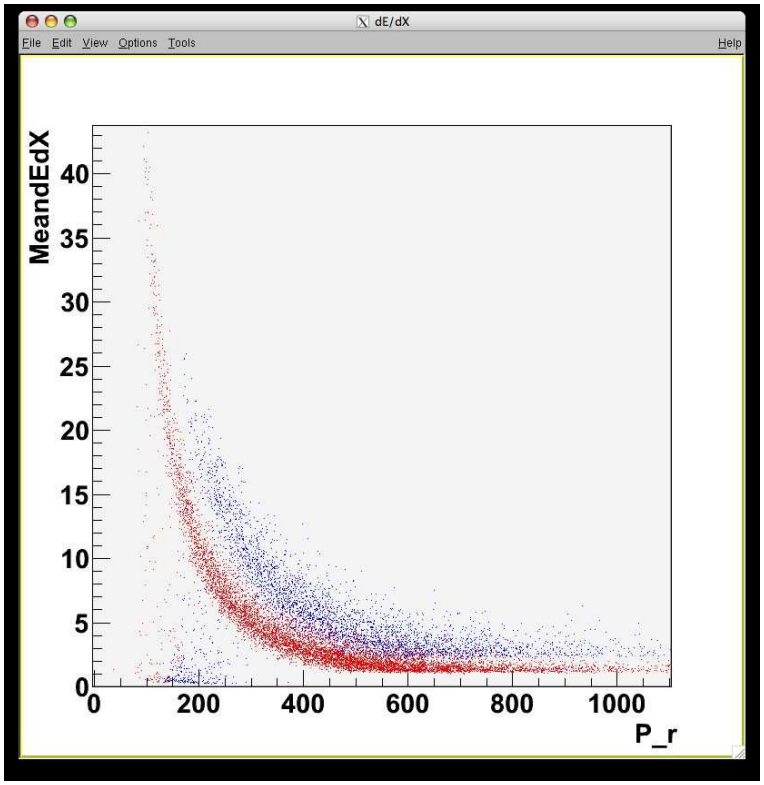

Figure 17: Monte-Carlo simulation of the energy loss as a function of momentum for alpha particles inside the RTPC gas for a 80/20 mixture of helium/DME (red) and neon/DME (blue).

For the proposed experiment the higher resolution in dE/dx will allow a much cleaner separation of proton from pion and deuteron (plus heavier nuclei) background, and extend the momentum acceptance, because of high p detection efficiency even at lower dE/dx.

5.4 Custom Gas Electron Multipliers

Gas electron multipliers are 50 μm thick polyimide foils coated on both sides with a 5 μm copper layer and punctured with 70 μm holes. The distance between these holes is about 140 μm. By applying a voltage in the range of 200 V to 300 V across the two copper layers a very high electric field is formed inside the holes. Electrons drifting towards the GEM foil produce an avalanche of secondary electrons when captured and accelerated through the holes. The gain is of the order of 100. The electrons are transferred to the next GEM foil and after passing three GEM foils the resulting electron pulse is detected on the readout plane. The three GEM support frames were dimensioned such that identical GEM foils of an active area of 20 cm $\times$ 17 cm could be used throughout. For the new BoNuS12 experiment

proposed here we will design a new layout of a continuous foil for each GEM plane cylinder. This will increase the azimuthal acceptance of the detector.

5.5 Readout Electronics

The outermost cylindrical layer of the detector is the readout board made out of a flexible polyimide substrate. It carries gold-plated conductive pads on the inner surface with a pattern of 4.45 mm × 5 mm, shown in Fig. 18. The pads are connected by closed vias to the outer surface on which groups of 16 pads are traced to a common connector, carrying 16-channel preamplifier cards.

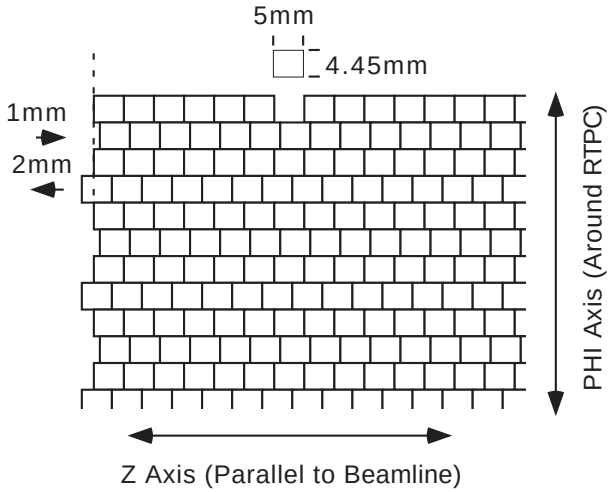

Figure 18: Pad Geometry in the Production RTPC. There are 40 rows and 40 columns of pads. Pad rows (along cylindrical axis) are offset from one-another to improve the track resolution.

The signals are inverted on these cards and transmitted via 6 m long cables to a low-impedance receiver circuit, feeding the positive signals into the readout electronics developed at CERN for the TPC of the ALICE experiment at the Large Hadron Collider for heavy-ion collisions [70]. Each readout card provides 128 channels of pre-amplification, digitization via a 10-bit ADC, signal correction circuits, and a pipeline buffer for eight events. Each event contains the signals of all pads integrated over 114 nsec time intervals for a period of 1.7 μsec before and 9.7 μsec after the arrival of an electron trigger from CLAS. Signals below preset thresholds, taking dynamically calculated and preset pedestals into account, are suppressed in the data stream to decrease the data volume for an increase of the event rate.

For the eg6 experiments the readout was grouped into six branches, each controlled by one readout controller (RCU), with four readout cards per branch. The readout controllers and communication cards had been purchased new after the 2005 data taking run to improve the data acquisition limit beyond 500 Hz. The ALICE standard readout hardware features fiber optical data links and controls, instead of the USB 2.0 connection used during BoNuS. During data taking of the eg6 experiments an event rate of 3 kHz was maintained with an electron beam current of about 120 nA.

5.6 Deuterium Target

The gas target used by the eg6 experiment consists of a Kapton tube, 6.0 mm in diameter with 30 μm thick walls, with entrance and exit windows located outside the length of the RTPC. The windows are made of 15 μm thick aluminum foil. The upstream entrance window is surrounded by an aluminum shroud to shield the RTPC from background particles created at this window. The shroud extends 47 mm into the inside of the RTPC and does not affect the acceptance for the low momentum recoil protons with large back scattering angles. The target cell can be filled up to a pressure of 7.5 atm with gas. Deuterium is the primary target gas, but also hydrogen and helium will be used for calibration purposes.

5.7 Some Results from the BoNuS 2005 Run

The BoNuS RTPC readout system consists of 3200 charge collection pads, each having 100 possible time bins in which to register a signal. Some of these hits may be eliminated as candidates belonging to a good track because they are outside of the physical area where a particle may travel. The first step towards the goal of clustering these hits together and identifying proton tracks is to have some knowledge of the paths on which ionization electrons travel before reaching the amplification and readout stages of the RTPC. The electric and magnetic fields inside the RTPC are neither parallel nor strictly perpendicular throughout the chamber volume complicating the track reconstruction. A proper description of the electron drift velocity vectors is needed before being able to describe a particle track.

Drift velocity vectors were calculated using the MAGBOLTZ program. In a first step, the electric and magnetic fields were determined and then used as input for MAGBOLTZ. The exact gas mixture during BoNuS data taking varied due to problems with the gas handling system. Seven different gas mixture configurations, varying between 72/25 and 85/15 were simulated.

Fig. 19 depicts a typical electron path in the drift region (30 mm to 60 mm radially), transfer and induction regions (between 60 and 69 mm radially) when produced at two different locations along the RTPC central axis.

Pattern recognition software was developed to link together hits that are close to each other in space into a chain. The algorithm starts by using every possible hit in the TPC as the seed from which a possible chain may grow. These chains are fit to a helix if the number of links in the chain is longer than ten.

The RTPC was calibrated by filling the target gas cell with hydrogen gas and detecting elastic scattering events with 1.1 GeV electrons. For this data taking the GEM amplification voltage was increased to make the RTPC sensitive to minimum ionizing particles. The electrons were then detected by the RTPC and CLAS, while the RTPC also detected the elastically scattered proton in the opposite hemisphere. The electron momentum and scattering angle determined the proton kinematics, which were compared to the directly measured proton momentum by the RTPC. An event display of such an event is shown in Fig. 20.

In Fig. 21 the difference between the vertex along the beam center line, and the difference between the scattering angles and the azimuthal angles as measured by CLAS and by the RTPC are displayed. The sigmas of the distributions are less than 1.5° for the scattering

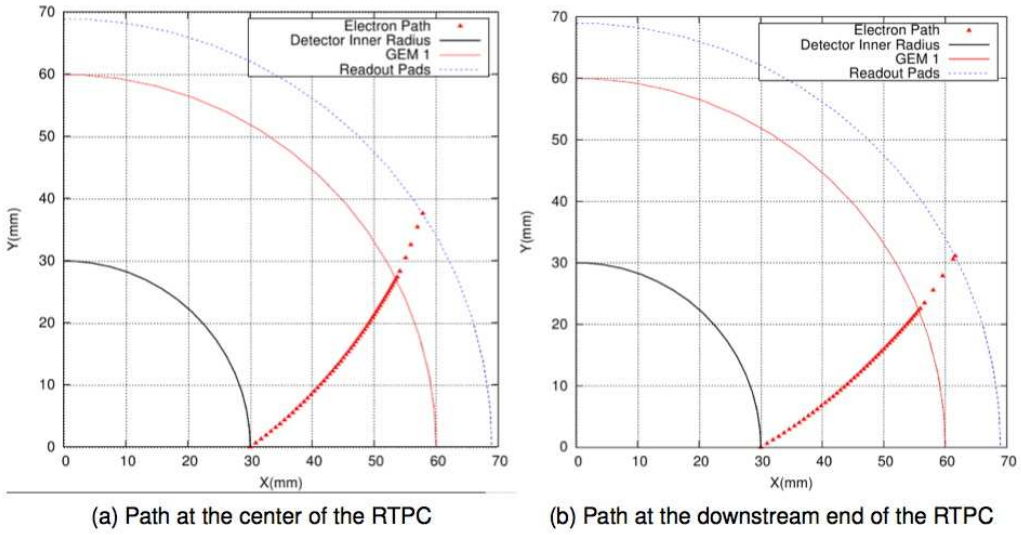

Figure 19: Two drift electron paths for different positions along the RTPC central axis are shown, starting at the cathode and ending on the readout pads. The red points shown are in steps of 100 ns. Note the effect of the Lorentz angle on the total azimuthal angle swept out by the paths.

angle and less than 5° for the azimuthal angle. The vertex position distribution has a sigma of 8 mm.

During data taking on the deuterium target, the electrons were only measured by CLAS, while the recoiling protons were detected by the RTPC. In Fig. 22 on the left, the correlation between electron and proton vertices is shown for 2.1 GeV beam energy.

After RTPC gain calibration the charge distributed by the particle passing through the detector can be used to calculate their energy loss while traversing the 3 cm drift region of the RTPC. For particle identification, this energy loss, dE/dx, can then be plotted versus the momentum fit of the particle track curvature shown in Fig. 23. Here the results from a special run for electrons with 2.1 GeV beam energy scattering off the target gas cell filled with helium are shown.

5.8 Some Results from the eg6 Experiment of 2009

The design of the newly developed RTPC for the eg6 experiment featured an improved mechanical support for the GEM foils and readout plane. The DAQ upgrade to the standard ALICE readout electronics was able to accommodate the data acquisition rate of 3 kHz.

The target gas used for the eg6 experiment was ^{4}He. This allowed the development of a new procedure for the calibration of the RTPC using low energy electrons of 1.2 GeV scattering of the helium target. Elastically scattered alpha particles were detected in the recoil detector, concurrently. Because of the high ionizing power of the alpha particless it is possible to use the same RTPC high voltages for calibration and production runs and, hence, avoids the need for extrapolations from the calibrated conditions to the running conditions.

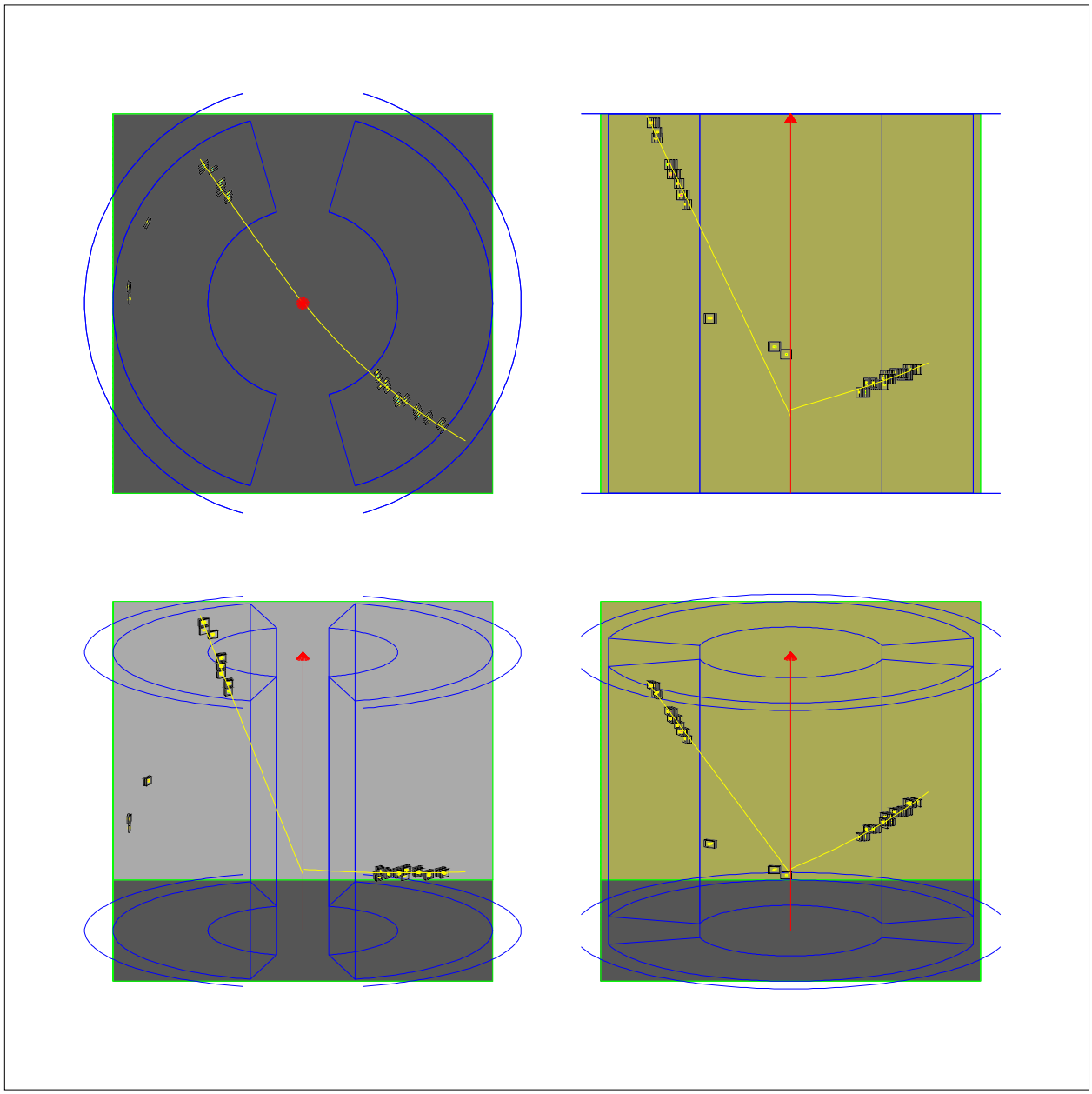

Figure 20: Elastically scattered electron (left) and proton (right) from a 1.1 GeV electron run on a hydrogen target. Top left: Cut perpendicular to the beam line (x-y-plane); top right: vertical cut (x-z-plane); bottom row: two 3D views, rotated 90° around the beam axis.

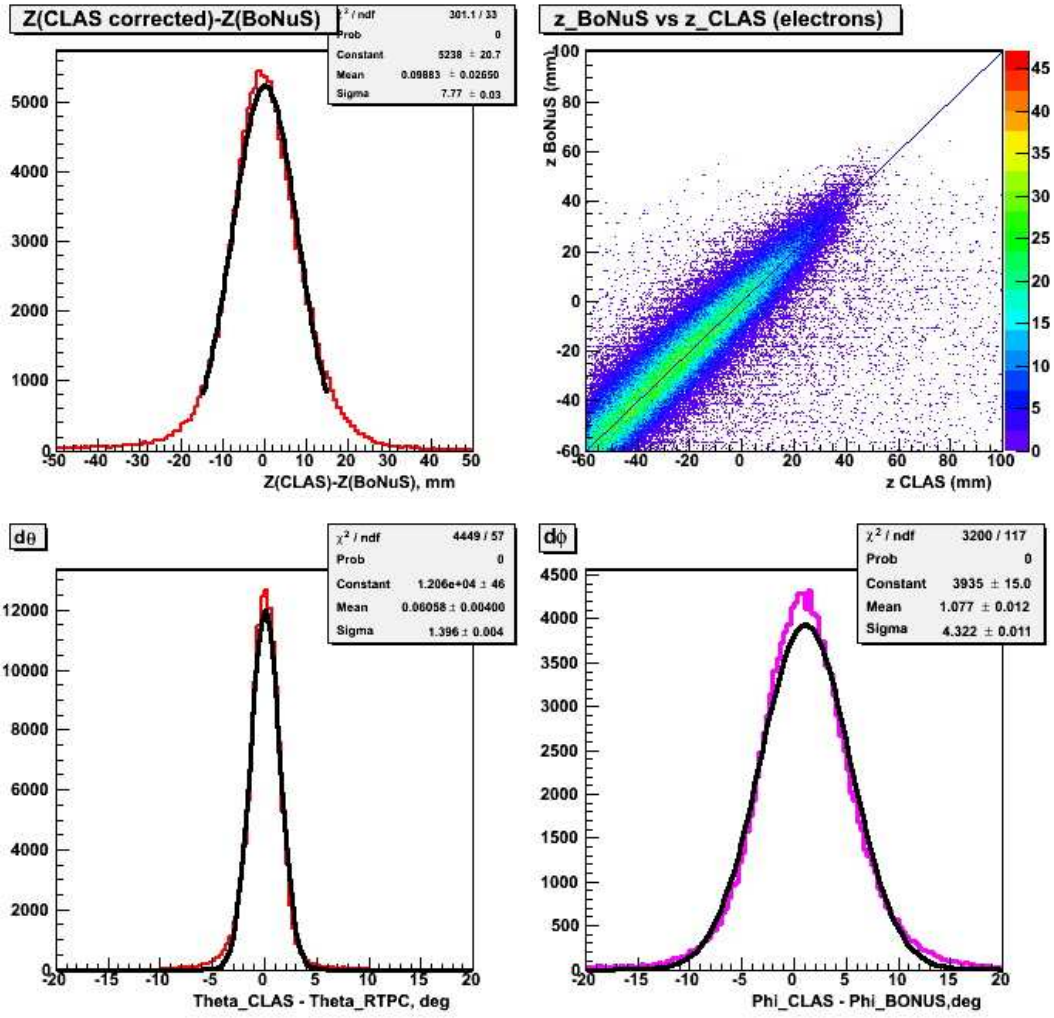

Figure 21: Difference between the electron vertex position, z (top row), the scattering angles, θ (bottom left), and azimuthal angles, ϕ (bottom right), as measured by CLAS and the RTPC using a hydrogen target and 1.1 GeV beam energy.

5.9 New RTPC Design Parameters

The design of the new RTPC for the BoNuS12 experiment has to accommodate a 40 times higher luminosity in comparison to the BoNuS experiment. An electron beam current of 200 nA will impinge on a 40 cm long gas target filled with deuterium gas a 7.5 atm pressure. The azimuthal coverage will be increased from about 300° to 350°. The vertex cut will be improved to ±5 mm because of the increased track length in the radially 4 cm long drift region, the increased signal strength because of the neon/DME gas mixture, and the new forward vertex detector of the central detector. The possibility of a new selective trigger, sensitive to electrons, would greatly suppress the background and increase the data rate.

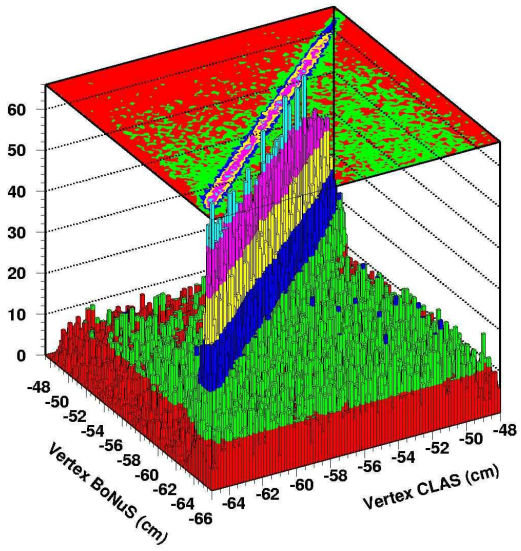

Figure 22: Vertex correlation plot between electrons as measured by CLAS and protons measured by the recoil detector.

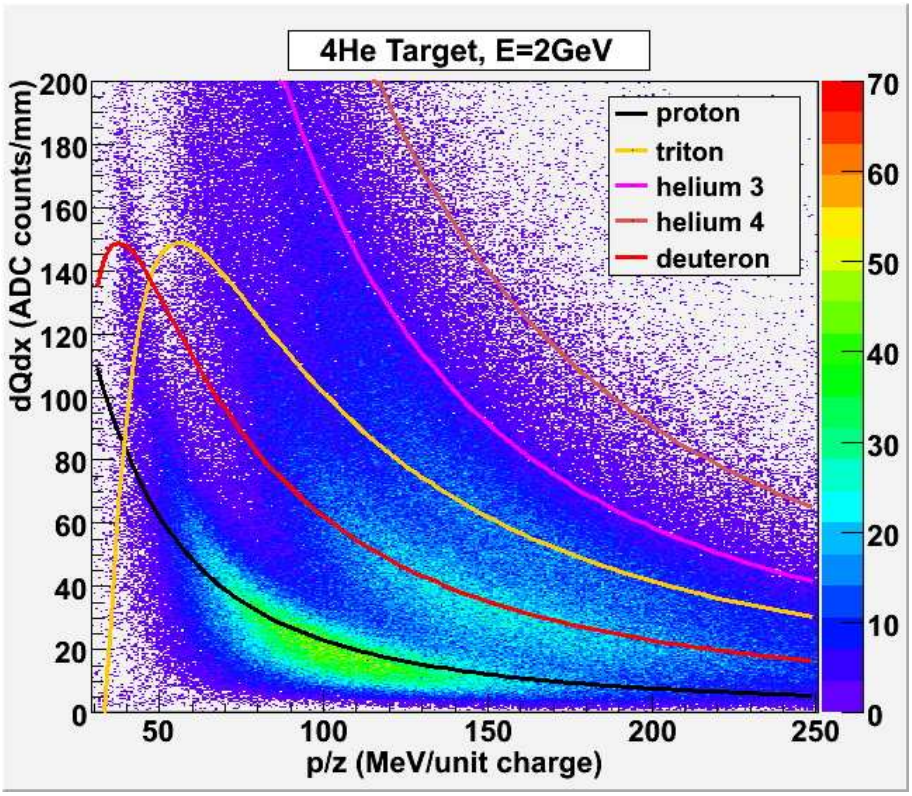

Figure 23: Fractional energy (charge) loss, dQ/dx, as a function of the fitted particle momentum divided by their charge for different nuclei. The data were taken with 2 GeV electrons scattering off a helium target.

6 Physics Results from BoNuS

6.1 Introduction

The Barely Off-shell Nucleon Structure (BoNuS) CLAS experiment ran in 2005 using a pioneering radial time projection chamber (RTPC), which tagged the spectator protons in electron-deuteron scattering. This experiment took data at 1.1, 2.1, 4.2 and 5.3 GeV beam energies, and measured the unpolarized structure function F_2^n over a wide range of kinematics. The most important results from this measurement are included below, since this proposal's goal is to extend the 2005 measurement to higher x and further into the deep-inelastic regime using CLAS12.

The BoNuS data were analyzed using two very different methodologies. In the first case, events tagged with a spectator proton in the RTPC were sorted into kinematic bins and normalized by the inclusive deuteron scattering events for the same kinematics. In this way, the problems of absolute normalization and CLAS acceptance were handled naturally by always dealing with experimental ratios and world parameterizations of known quantities such as the deuteron and proton cross sections. In the second case, only the tagged spectator events were used, but the binned data were compared directly to a Monte Carlo simulation of CLAS with events generated according to a plane-wave impulse approximation (PWIA) spectator model. In this case the ratios were of data to simulation in contrast to the ratios of data to data in the first case.

Both methods produce consistent results and exemplify the success of the tagging technique to measure the free neutron's structure using neutrons bound in nuclei.

6.2 Accidentals, Acceptance and Efficiency

Using the first methodology, the experimental quantity of interest is the ratio of electron scattering events tagged by a spectator proton and untagged, corresponding to inclusive *ed* scattering. Once corrected for backgrounds and efficiency, this tagged to untagged ratio equals the structure function ratio F_2^n/F_2^d, provided that the R structure function for the neutron and the deuteron are identical. In order to reduce the effects of final-state interactions and off-shell effects, the spectator momentum was chosen to be $0.07 < p_s < 0.10$ GeV and the spectator angle with respect to the momentum transfer was chosen to be $\theta_{pq} > 110°$.

Coincidence events with an electron measured in CLAS and a spectator proton measured in the RTPC are confirmed by comparing the position z along the beam line of track origins. Fig. 24 shows the spectrum of $z_{\mathrm{CLAS}} - z_{\mathrm{RTPC}}$. The large central peak corresponds to true coincidences, and the background on either side corresponds to accidental electron-proton coincidences. The z distributions for electrons and protons are flat over the 28 cm length of the target. Therefore, the convolution of these two distributions gives rise to a triangular background spectrum. By fitting the background and peak, one can collect events that fall within and outside of the blue limits. A simple multiplicative factor R_{bg} scales the background events to correspond to the number under the peak.

The relative CLAS electron acceptance was determined for bins in Q^2 and W using the ratio of observed inclusive scattering rates off the deuteron compared to the radiated model of Bosted and Christy[71, 72] derived from global fits to the world's data. Fig. 25 shows the

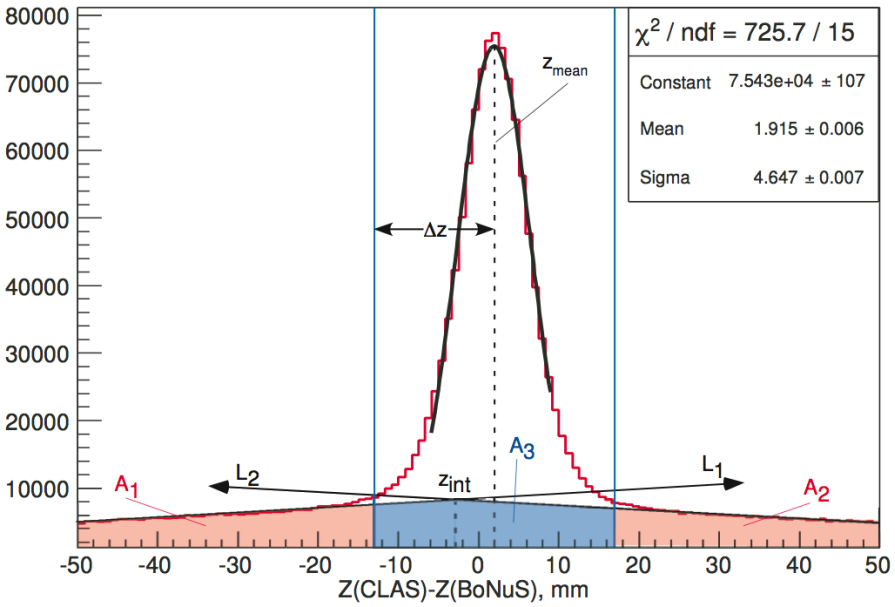

Figure 24: Distribution of Δz, the difference between the reconstructed track position along the beam direction of electron and spectator proton. The peak shows coincident events between CLAS and the RTPC. Accidental coincidences appear in the wings.

dependence on W for four Q^2 bins. The top graphs (blue) are the inclusive data, the middle graphs (black) are the model, and the bottom graphs (red) are the ratio of the two, which is the relative electron efficiency, $\epsilon(W, Q^2)$ for CLAS.

The tagged/untagged ratio, corrected for CLAS acceptance, was determined using:

$$R_{corr} = \frac{\sum_{i=1}^{N_{tag}(W^*,Q^2)} \frac{1}{\epsilon_i(W,Q^2)} - R_{bg} \sum_{j=1}^{N_{bg}(W^*,Q^2)} \frac{1}{\epsilon_j(W,Q^2)}}{\sum_{k=1}^{N_{untag}(W,Q^2)} \frac{1}{\epsilon_k(W,Q^2)}} \tag{18}$$

in which each tagged or untagged event is weighted by the efficiency. The first sum in the numerator corresponds to events in the trues coincidence peak between CLAS and BoNuS, whereas the second sum corresponds to events that fall outside the trues peak. The factor R_{bg} scales the background to correspond to that underneath the trues peak. The variable W^* corresponds to the spectator-corrected true center-of-mass energy of the struck neutron, and several bins in W can contribute to a single bin in W^*.

This treatment does not account for the efficiency of the RTPC. Because of the difficulty of accurately simulating the BoNuS detector efficiency, the tagged/untagged ratio was normalized to the world's data for $x = 0.35$, $W > 2.0$ GeV and $Q^2 > 1.0$ GeV^2, where neutron structure functions can be reliably extracted from deuteron data. Here, the single constant n was used for all kinematic bins.

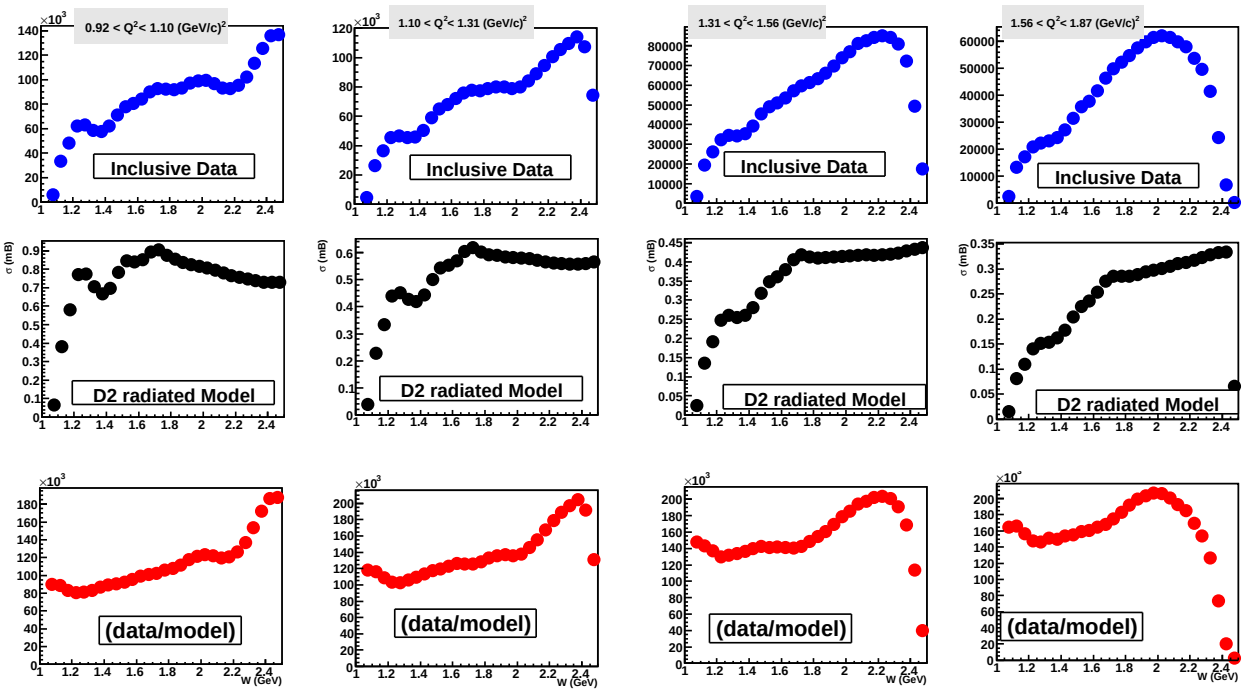

Figure 25: The total inclusive electron scattering counts for deuterium (top row), the total radiated deuteron cross section model provided by P. Bosted [71] and E. Christy [72] (middle row) and the ratio of data to model. The plots are all versus invariant mass, W. Each column corresponds to a different Q^2 bin (only the $E_{beam} = 4$ GeV data are shown).

6.3 Pion and Charge Symmetric Background Contamination

Corrections for pion background and pair symmetric contamination were made using the CLAS EG1B parameterizations of N. Guler [73]. The EG1B π^-/e^- and e^+/e^- ratios are expected to be similar to those of the BoNuS experiment at the same kinematics. The two ratios r_{NH_3} and r_{ND_3}, for ammonia and deuterated ammonia targets were combined to yield ratios for the neutron, proton and deuteron. Both pion and pair-symmetric corrections are small. Fig. 26 shows the correction factor $(1 - r_n)/(1 - r_d)$ in which r is the π^-/e or e^+/e^- ratio for a neutron (n) or deuteron (d) target. Although the correction grows substantially with W, it remains small over all kinematics, and the systematic errors on these corrections are far less than 1%.

6.4 Radiative Corrections

Radiative corrections to the tagged/untagged ratios were calculated using the cross section models of P. Bosted [71] and E. Christy [72] within the formalism of Ref. [74]. The correction takes the form of a super-ratio

$$r_{rc} = \frac{\sigma^n_{Born}/\sigma^n_r}{\sigma^d_{Born}/\sigma^d_r} \tag{19}$$

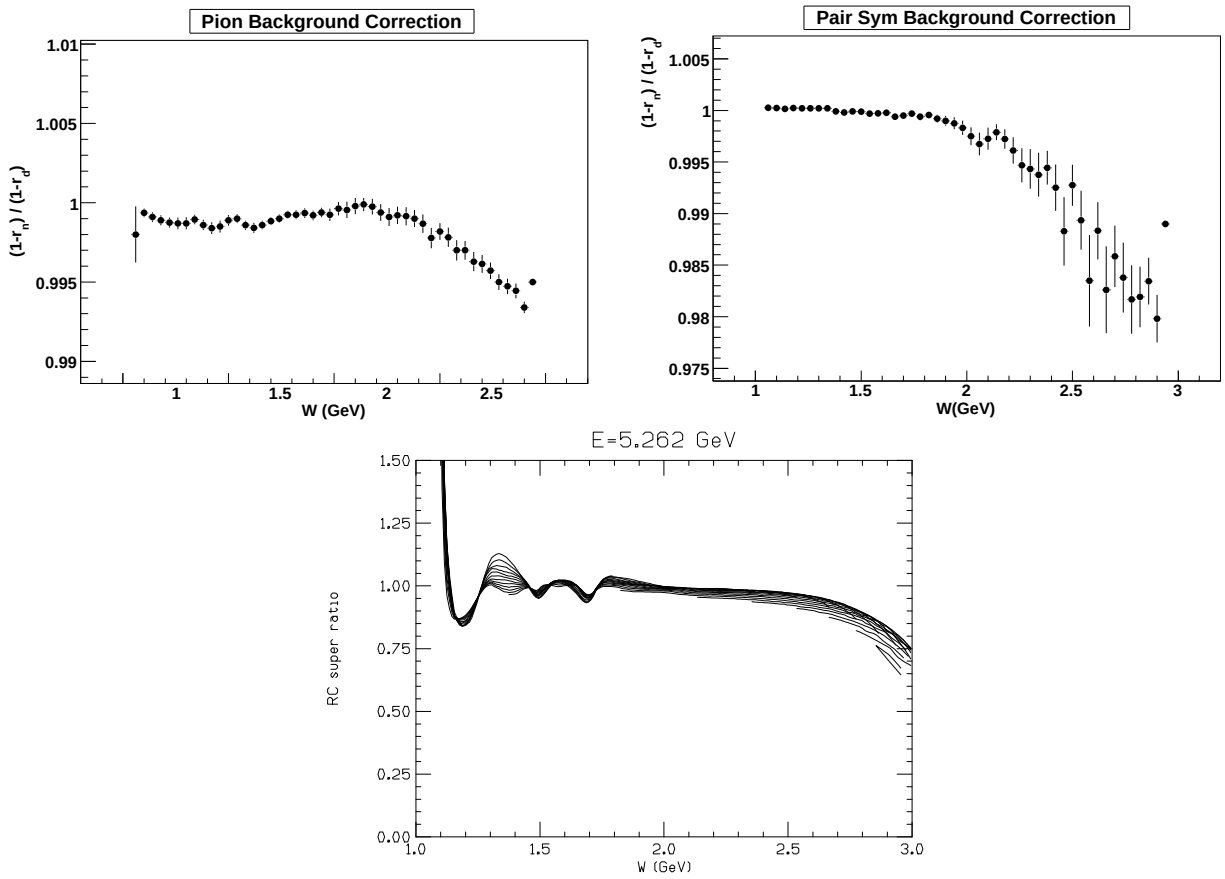

Figure 26: The correction to the tagged/untagged ratio due to π^- contamination (left), pair-symmetric background (right) and radiative effects (bottom).

in which σ^n and σ^d correspond to cross sections for neutron and deuteron targets, respectively, and σ_{Born} and σ_r correspond to the Born and radiated cross sections, respectively. The BoNuS target was 0.04 radiation lengths. Cross sections were generated in the same bins of W and Q^2 as the experimental tagged/untagged ratios. Kinematic regions where the (quasi-)elastic radiative tail was greater than 10% were excluded. Fig. 26 shows $1/r_{rc}$ as a function of W for various values of Q^2. Data below $W = 1.1$ GeV were excluded because of large radiative corrections from (quasi-)elastic scattering.

6.5 Structure Function Ratio Extraction

A sample of the untagged and tagged distributions can be seen in Fig. 27. Clearly, the calculation of the proper invariant mass of the neutron, W^*, sharpens the quasi-elastic peak and the resonances begin to take shape as we would expect from inclusive scattering on a free nucleon. Since W^* is always less than W for backward-going spectator protons, there is a steep fall off to the tagged/untagged ratio at the edge of the experiment's W acceptance. This is an unavoidable result of the kinematics and can be removed with a simple Q^2-dependent cut on the maximum invariant mass.

The structure function ratio F_2^n/F_2^d versus W and Q^2 can be determined directly from

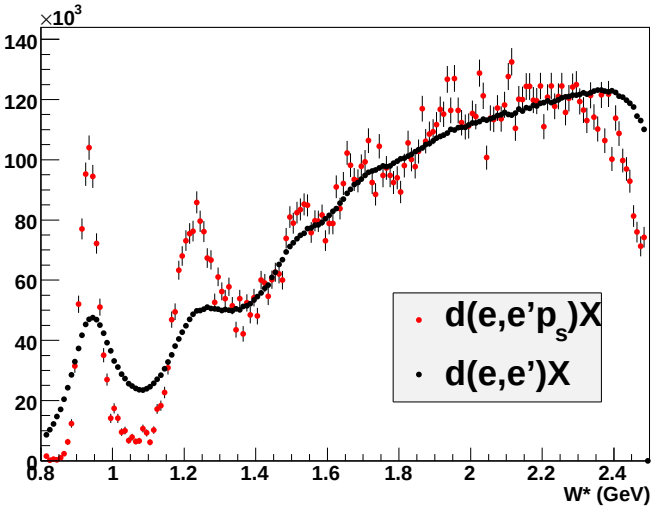

Figure 27: Inclusive scattering on deuterium (black line) representing our untagged data sample as a function of W and the corresponding tagged sample as a function of the corrected mass W^*. The data are normalized so that the area under the curves is equal. $E_{beam} = 4.223$ GeV

the corrected tagged/untagged count ratio $R_{\rm corr}$:

$$\frac{F_2^n}{F_2^d} = nC_{e^+}C_\pi r_{rc}R_{corr} \tag{20}$$

in which n is the RTPC efficiency correction, C_{e^+} and C_π are the pion and pair symmetric contamination corrections, and r_{rc} is the radiative correction super ratio. Then

$$\frac{F_2^n}{F_2^p} = \Big(\frac{F_2^n}{F_2^d}\Big)\Big(\frac{F_2^d}{F_2^p}\Big)_{\rm model}. \tag{21}$$

using good parameterizations of the world's data on the proton and deuteron to scale the ratio. Multiplying Eq. 21 by $F^p_{2(\rm model)}$ yields F_2^n.

6.6 Error Estimation

The statistical error on the acceptance corrected counts is simply

$$\sqrt{\sum_{i=1}^{N} \frac{1}{\epsilon_i^2(W,Q^2)}} \tag{22}$$

for each summation in the numerator and denominator. These errors are properly propagated through to give the total statistical error on R_{corr} in Eq. 18. Estimates of the systematic errors on each of the multipliers in Eq. 20 are 5% for final-state interactions, 1% from target fragmentation for spectator kinematics, 1% for off-shellness, $< 1\%$ for pair-symmetric and π^- backgrounds, 2% on the radiative correction, 4% on the model cross section ratios, and

5% from the assumption of flat BoNuS efficiency versus W. The total systematic error is about 9%. Ongoing studies of these errors will reduce them further, especially errors on the W-dependence of the BoNuS efficiency.

6.7 Sensitivity to Spectator Momentum

In order to ensure that our tagged spectra are not significantly distorted by final-state interactions or off-shell effects, we have studied the effective neutron structure function $F_{2\text{eff}}^n$ as a function of the spectator proton momentum p_s and the spectator scattering angle θ_{pq}. To do so the second method of data analysis was employed, constructing the ratio of the raw experimental $d(e, e'p_s)$ data and a full Monte Carlo simulation of the pure spectator model that includes the detector acceptance, efficiency, binning, subtracted accidental background, and the radiative elastic tail. Multiplying this quantity by the model structure function used in the Monte Carlo simulation yields $F_{2\text{eff}}^n$, which may be differ from F_2^n because of final-state interactions and off-shell effects.

In this case, systematic errors arise from the accidental background subtraction, CLAS acceptance and efficiency (9%), cross-normalization (10% at 5 GeV), and model-dependence in the Monte Carlo simulation. Individual systematic errors are added in quadrature.

Fig. 28 shows the tagged event rate as a function of $\cos\theta_{pq}$, normalized by the Monte Carlo expectations from a pure spectator model. Deviations from unity indicate the effects of final-state interactions and off-shell effects. These data are at a moderate Q^2 of 1.66 GeV^2, and $W^* = 1.73$ near the third resonance region. For $p_s = 0.08$ and 0.10 GeV, there is little indication of deviations from the spectator picture, even at forward angles. However, for $p_s = 0.12$ and 0.14 GeV, still relatively low momenta, one finds a depletion perpendicular to the momentum transfer, which is a signature of final-state interactions, since the most likely np interaction is a grazing blow as the neutron moves largely in the direction of momentum transfer. This plot confirms that by limiting the spectator momenta to the range $0.07 < p_s < 0.1$ GeV, especially with a cut on backward angles, one observes a quasi-free neutron with small off-shell and final-state interaction corrections.

Fig. 29 shows F_2^n as a function of W^*, again for $Q^2 = 1.66$ GeV^2, but for backward-going spectators with $-0.75 < \cos\theta_{pq} < -0.25$. There is very little difference in F_2^n as p_s increases from about 0.08 GeV (upper left) to 0.14 GeV (lower right). Especially in the deep-inelastic region, $W^* > 2$, there is no statistically significant evolution of the structure function with p_s. Hence, we can be confident that data with $0.07 < p_s < 0.10$ are not noticeably marred by either final-state interactions or off-shell effects.

Since the p_s resolution was about 10%, there is some mixing in the chosen p_s bins. The poorly understood momentum-dependent efficiency of the RTPC made it necessary to cross-normalize the experiment and simulation separately for each p_s bin. This could hide systematic offsets of these ratios from unity, and, consequently, mask systematic deviations of $F_{2\text{eff}}^n$ from the model F_2^n.

These results tend to agree with the target fragmentation model of [44], and the final state interaction model of [64]: our data are enhanced over the PWIA in the target fragmentation region (in accordance with [44]) and dip in the vicinity of $\theta_{pq} = 90^\circ$ (in accordance with [64]). The PWIA spectator model works well for the lowest spectator momentum bin (p_s=70. . .90 MeV/c), as expected from the models of [49] and [51], especially in the backward θ_{pq} region.

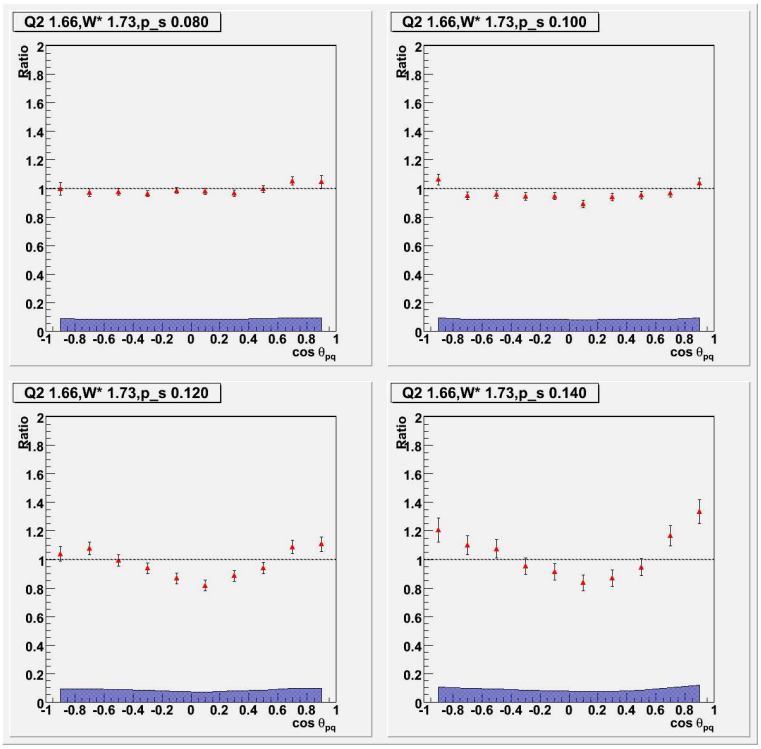

Figure 28: Ratio of experimental data with subtracted accidental background and elastic tail to the full simulation in the PWIA spectator picture as a function of $\cos\theta_{pq}$. Data are for $Q^2 = 1.66$ GeV^2 and $W^* = 1.73$ GeV. The beam energy is 5.254 GeV. Error bars are statistical only. Systematic errors are shown as a blue band.

The resonance-like structure present in the ratio of the experimental data to the simulated data 29 shows that our model for F_2^n may underestimate the resonant contribution at some values of W^* and Q^2. On the other hand, the agreement between data and model for the 2 highest Q^2 bins at 5 GeV, over the whole range in W^*, is quite good in the region where the spectator picture should work (p_s between 0.07 and 0.10 GeV and $\cos(\theta_{pq})$ between -0.75 and -0.25). This confirms that in the DIS region, the F_2^n model provides a good description of a (nearly) free neutron up to $x^* \approx 0.6$, within our systematic errors of 10 - 15%. Here, x^* is the kinematically corrected Bjorken x.

Some uncorrected reconstruction and efficiency effects for CLAS and the RTPC limited our resolution in W^*/x^* and they have washed out some of the details. A larger statistics run using CLAS12 and an improved RTPC will improve these data and extend them to higher Bjorken x.

6.8 F_2^n/F_2^d, F_2^n/F_2^p, and F_2^n

Representative results for F_2^n/F_2^d, F_2^n/F_2^p and F_2^n from the measured and corrected tagged and untagged ratios, following the prescription of Eq. 20, are shown in Fig. 30. The panels contain the structure function ratios and F_2^n as a function of W^* and x^*, for $Q^2 = 0.84$ GeV^2.

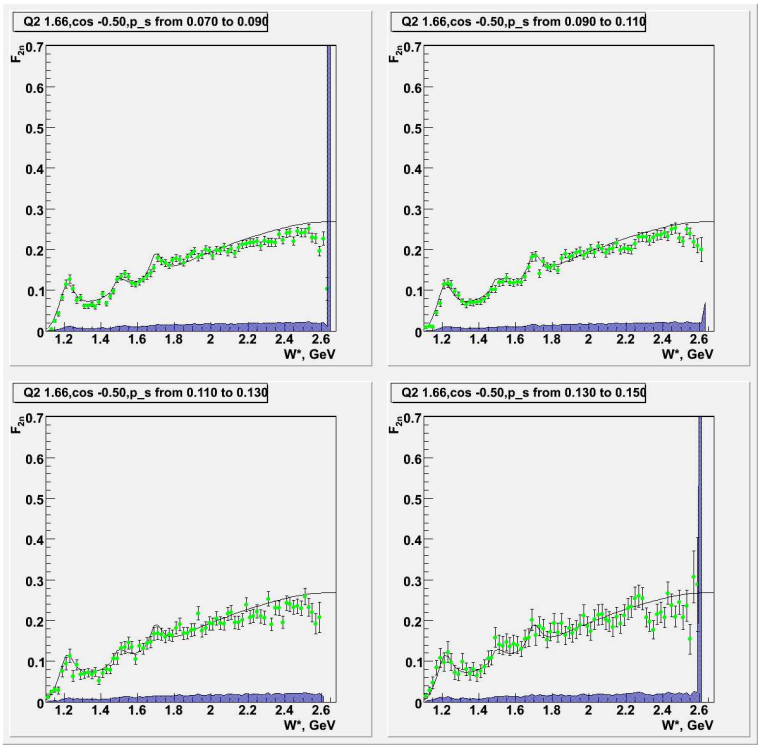

Figure 29: Effective (green points) and model (red line) F_2^n structure functions versus x^*. Data are for $Q^2 = 1.66$ GeV^2 and $\cos\theta_{pq}$ from -0.75 to -0.25. The beam energy is 5.254 GeV. Error bars are statistical only. Systematic errors are shown as a blue band.

The model of Refs. [71] and [72] is shown as the curve. Since this model was constructed from the world's data on nuclear targets, one might expect deviations with the present data set on a nearly unbound neutron.

Fig. 31 shows a comparison of F_2^n versus x^* obtained with the same data set, but the two alternative analysis methods. These points are summed over Q^2 for $W > 1.8$ GeV. They agree quite well with each other, and their deviations from each other help quantify the differing systematic errors in the two methods.

Fig. 32 shows the structure function ratio F_2^n/F_2^p versus x^* from the BoNuS experiment. Since this ratio does not evolve quickly with Q^2, we have included all Q^2 values above 1 GeV^2 in each x-bin. The different colored points show the effect of cutting into the resonance region where $W^* < 2$ GeV. If duality holds, the different Q^2 values contributing will wash out any resonance structure and we would expect the average ratio to follow the deep-inelastic trend. However, there is clearly an effect at $x = 0.65$, which corresponds to resonance structure around $W^* = 1.7$ GeV. The black points, and the off-resonance red points follow the CTEQ trend, suggesting that the n/p ratio takes the middle road as $x \to 1$.

With the spectator tagging technique a demonstrated success, it is clear that a repeat experiment that pushes to higher x in the deep-inelastic regime is strongly desirable.

The soon to be published BoNuS physics results have been presented already at conferences, including the annual Jefferson Lab Users Meeting in June 2010. The preparation of a

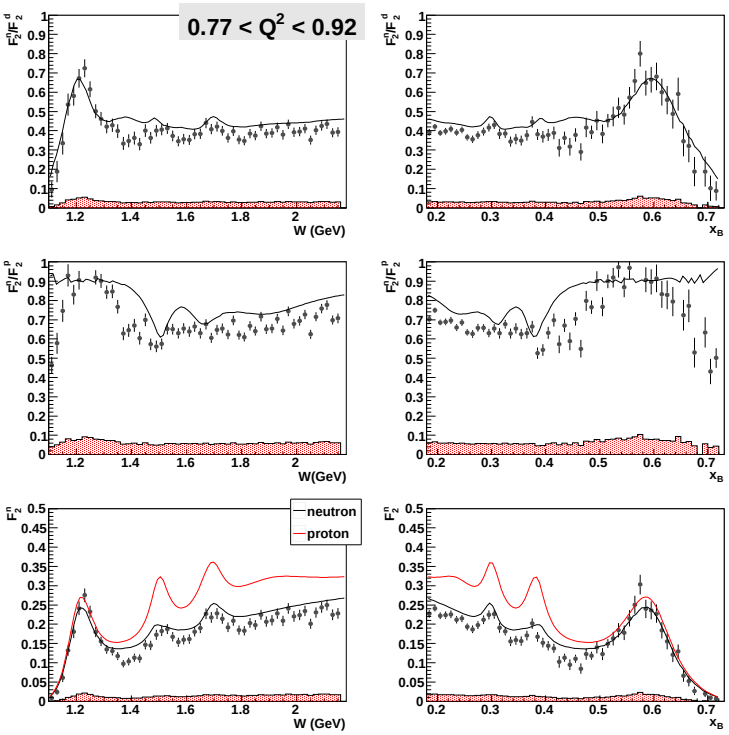

Figure 30: F_2^n/F_2^d, F_2^n/F_2^p, and F_2^n versus W and x at $1.31 < Q^2 < 1.56$ GeV^2, $E_{beam} = 5.262$ GeV. The neutron and proton lines are from the phenomenological model of Refs. [71] and [72].

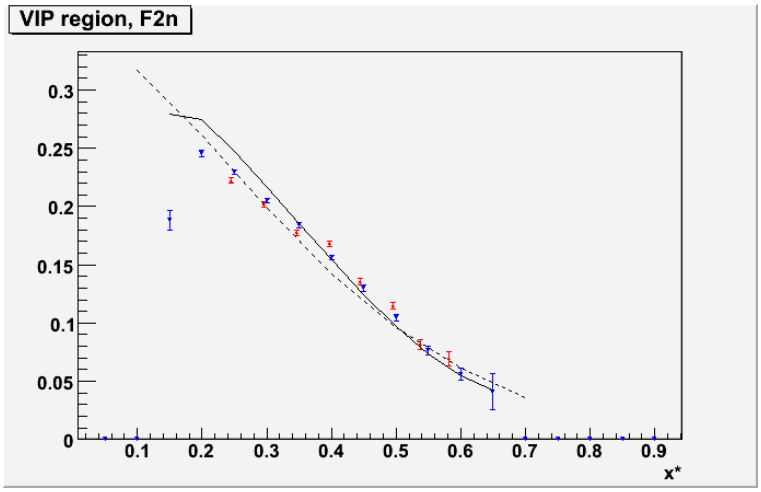

Figure 31: The BoNuS experimental F_2^n versus x derived from the two independent analyses of the same data set. The small differences between the two methods bound the systematic errors that differ between them. Red points correspond to the tagged/untagged ratio method and blue points correspond to the tagged to Monte Carlo ratio method.

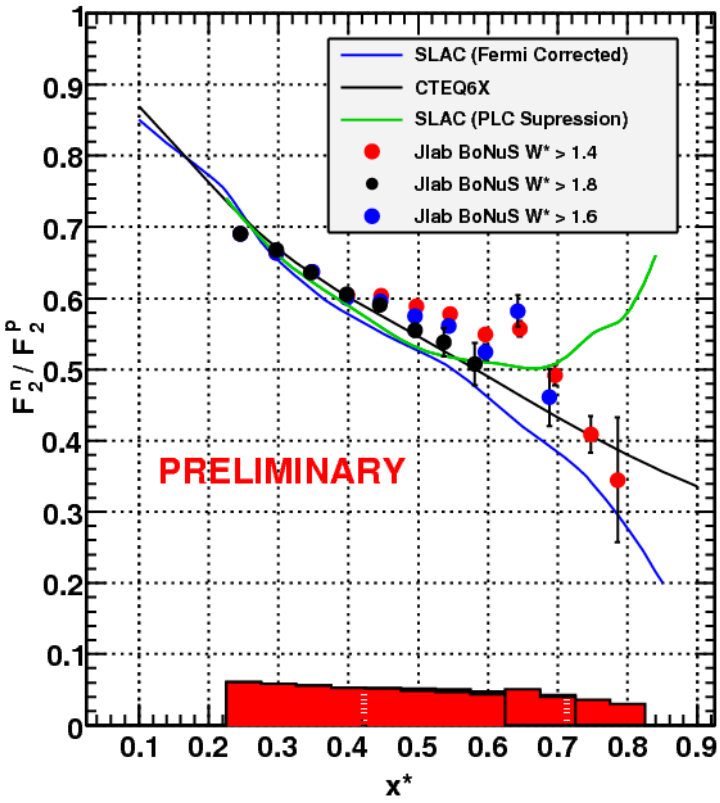

Figure 32: The ratio F_2^n/F_2^p versus x. The SLAC deuteron data are from [75] and [76], with corrections for Fermi motion only (blue curve) or for point-like nucleon configurations based on Ref. [10]. The black curve corresponds to the best CTEQ structure function fits at high x. The BoNuS data are from the E_{beam} =5.262 GeV run period, with statistical uncertainties shown on the points and total (correlated) systematic uncertainties shown in the error band on the bottom of plot. The colored points indicate cuts on W^* above 1.4 GeV (red), 1.6 GeV (blue) and 1.8 GeV (black).

CLAS analysis note is well underway, two PhD theses have been published [2, 3], and a paper draft for publication is about to be circulated within the CLAS collaboration for review. A technical paper describing the recoil detector and it's behaviour has been published [67].

7 Expected Results

In this section, we describe the details of our simulation of the proposed BoNuS experiment. In particular, we show that we can achieve sufficient resolution in all relevant kinematic variables and adequate statistical and systematic precision for the kinematic bins of interest.

7.1 Monte Carlo Simulation

We developed a Monte Carlo simulation for the proposed experiment to determine expected count rates, kinematic coverage and resolution. The event generator for this simulation [77]

uses a parameterization of the world's structure function data on protons and deuterons and a realistic model of the deuteron momentum wave function (based on the Paris potential and the light-cone prescription by Frankfurt and Strikman [43]) to produce electron–backwards proton coincident events distributed according to the PWIA cross section in the spectator picture. This event generator has been shown to represent quite well the JLab E6 data taken at higher spectator momenta in the backward region [77], as well as the existing BoNuS data (see previous section). The generated events were randomly distributed along the central (z) axis.

The backward–scattered spectator protons having an initial momentum greater than 60 MeV/c were followed through the simulation of the target and RTPC. Both energy loss and multiple scattering in all components of the target and detector were taken into account, as was the curvature of the track in the solenoid field.

A simulation of the BoNuS RTPC was set up which includes proper electric and magnetic fields to correctly account for the drift of the ionization electrons in the RTPC's active volume. The proton track parameters were processed by this package to produce simulated RTPC signals. These signals were used by the RTPC analysis package to attempt reconstruction of the proton tracks. For each successfully reconstructed proton, the resulting 4-momentum and a flag indicating that the proton was detected in the RTPC were written to an output file.

Similarly, the corresponding electron trajectories were processed by a modified version of the new CLAS12 simulation package *clasev*. The scattering-angle coverage used for the forward detector was from 5° to 35°. The new CLAS12 central detector was not included in the simulation, as it would be replaced by the RTPC for this experiment. These two simulate–analyze chains were finally combined to yield meaningful predictions of event yields, acceptance, and experimental resolutions.

For the final data sample discussed below, we considered only protons with initial momentum below 100 MeV/c and with a scattering angle of more than 90° relative to the beam and more than 110° relative to the direction of the momentum transfer vector. These very important protons (VIPs) correspond to scattering events off nearly on-shell neutrons, with very little uncertainty from final state interactions and off-shell effects (see Section 3). Fig. 33 shows the spectator momentum acceptance of the proposed experiment according to our simulation.

It is important to note that we will be able to separate pions from protons in the RTPC detector up to momenta of at least 200 MeV/c by comparing the track curvature in the solenoid field and the energy loss in the active detector volume. We will thus be able to make a direct connection with the momentum range covered by the standard CLAS12 central tracker, which will allow us to study in detail the onset of off–shell effects and other deviations from the simple spectator picture in a future extension of E6 to 11 GeV, and to pin down the extrapolation curve shown in Fig. 12 at the high momentum end.

7.2 Resolution

In the proposed experiment, we will use the track curvature in the solenoid field to separate protons from pions with similar energy deposit (and therefore much lower momentum) in the active detector region. On the other hand, we can use the deposited energy to calculate

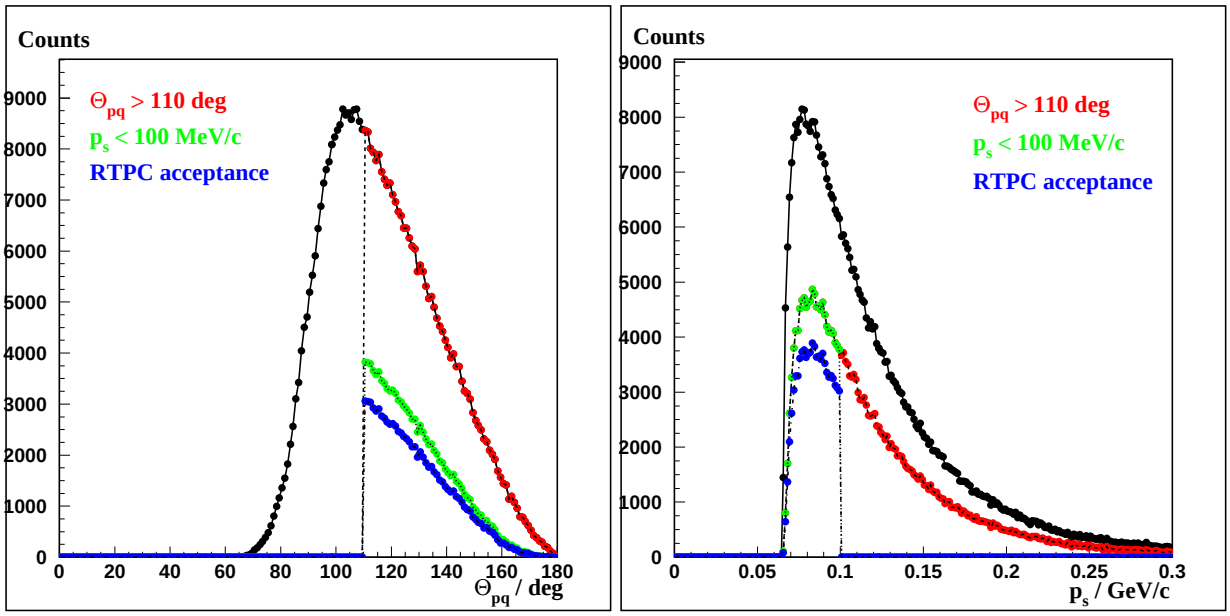

Figure 33: Influence of cuts on the expected number of counts for the proposed experiments of running at 11 GeV, plotted as a function of the angle between the spectator direction and the **q** vector, θ_{qp_s}, (left) and as a function of the spectator momentum p_s (right). Cut 1 (black points) contains all events where an electron is detected within fiducial cuts and a proton is emitted at more than 66 MeV/c momentum and at more than 90° scattering angle with respect to the beam direction. Cut 2 (red points) requires additionally that θ_{qp_s} is more than 110°. Cut 3 (green points) requires additionally that the spectator momentum is below 100 MeV/c and the final cut 4 (blue points) requires that the spectator is detected within the acceptance of the recoil detector.

the initial momentum of the proton (once its identity has been established). With a 25% resolution on the deposited energy, we can achieve a resolution $\Delta p/p = 10\% \times (p/100\,\mathrm{MeV}/c)$, more than sufficient for the purpose of kinematic corrections for the initial state motion of the unobserved neutron. If we assume as a worst–case scenario that the resolution on both the track beginning and track end in the 4 cm active region is determined by the longitudinal pad size, $\sigma_z = 5\ \mathrm{mm}/\sqrt{12}$, we can still extrapolate the proton vertex to about 3 mm resolution, even including multiple scattering. On average 15 pads will contribute to the determination of each track, making the vertex resolution sufficiently narrow to apply a ±5 mm vertex cut to eliminate accidentals. This will yield a suppression of about a factor of 80 for accidental coincidences by requiring the proton and electron vertices to be within 5 mm of each other. Additionally, the timing resolution of 500 ns will reject out of time tracks. Once a proton has been identified as being in true coincidence with a scattered electron, we can use the superior electron vertex reconstruction of CLAS12 with the forward vertex tracker (FVT) and the average track position inside the TPC to determine the scattering angle to about 3°. The resolution in ϕ will be even better due to the narrow beam width and the smaller pad size in that direction. We expect a similar accidental rate as in BoNuS in spite of the much higher luminosity.

Taken together, we will resolve the initial backward proton momentum to substantially

better than 10 MeV/c and the relative angle between the direction of $\mathbf{q}$ and the proton to about 2°. This results in an additional uncertainty on the reconstructed missing mass W of the unobserved neutron of about 11 MeV at the elastic peak and less at higher W, clearly much better than the expected intrinsic CLAS12 resolution.

7.3 Background Events

The largest *potential* source of background events comes from Møller electrons. Most of these electrons are produced at very forward angles, where they miss both the RTPC and the forward vertex tracker (FVT) completely, or at rather large angles and low momenta, easily "curled up" by the 5 Tesla solenoid field. A detailed simulation (see Fig. 34) shows that electrons produced along the front half of the target at angles as low as 4° (corresponding to 200 MeV/c momentum) get bent back towards the beam line and remain within a cylindrical volume of radius 2 cm, well outside the RTPC sensitive volume. At even smaller angles, they are still focused enough by the solenoid field to miss both the RTPC and the opening in the FVT. Most high-momentum Møller electrons are moving with angles less than 0.4° relative to the beam direction throughout the deuterium gas target, thereby also missing the (comparatively much more dense) target walls.

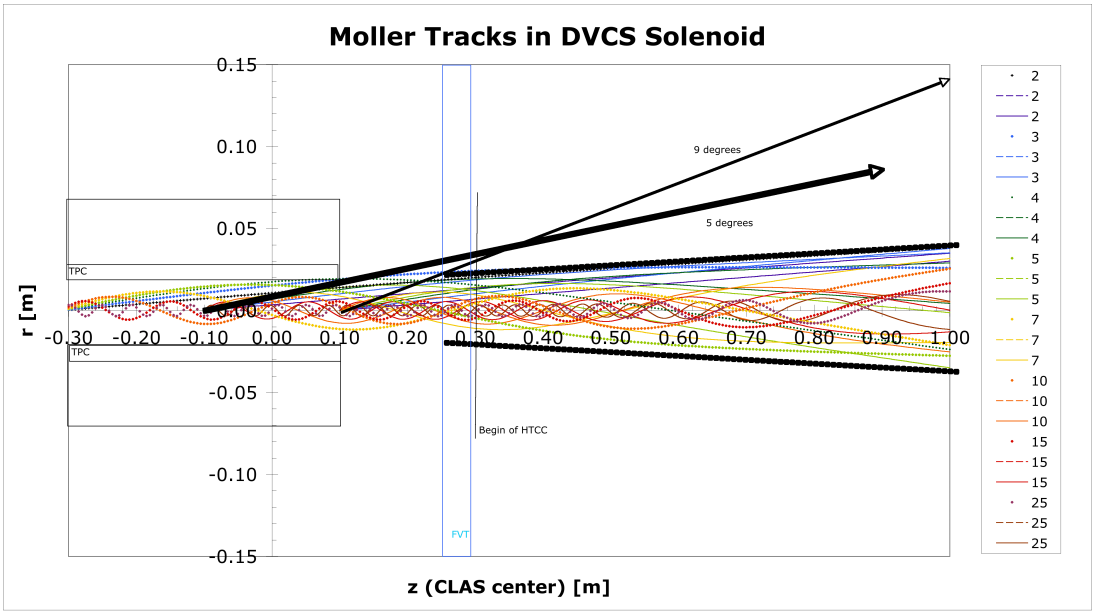

Figure 34: Simulation result of Møller electron trajectories curling around the beam solenoid (beam) axis in forward direction. The cone of trajectories clears both the drift region and even the standoff between ground plane (innermost foil) and cathode plane (at 3 cm radius) of the RTPC, as indicated by the outline overlaid on top of the tracks. The position along the beam line of the forward vertex tracker is shown as a blue outline. The dotted black lines indicate the "stay clear zone" where no detectors or other beam line elements intrude.

Assuming that the target occupies the range from -30 cm to +10 cm along the beam line (relative to the solenoid center), Fig. 34 indicates that with the standard location of the

forward tracker elements (including FVT and high threshold cherenkov counter, HTCC), we preserve a minimum scattering angle of less than 5° on average and 9° maximum, while avoiding any direct hits of detector elements (including the RTPC) by Møller electrons. Indeed, all Møller electrons will be contained in the same cone as was assumed for the design of the standard Møller shield cone for CLAS12 (indicated by the dotted black lines). Secondary electrons and photons may create a small background in the RTPC, but because of the insensitivity of the RTPC to minimum ionizing particles, electrons will not lead to any "fake tracks", and photons only leave single point-like charge deposits (less than one on average during any coincidence window). These conclusions are confirmed by a detailed simulation of electromagnetic backgrounds by A. Vlassov. In the region around the beam line occupied by the RTPC the integrated rate of all electromagnetic background is below 160 kHz for a luminosity of $2 \cdot 10^{34}$ cm^{-2}sec^{-1}, most of it invisible to the RTPC detector. Similar simulations where done for the original BoNuS experiment and were confirmed by our experience.

A second type of background comes from pions and heavier nuclear fragments that enter the RTPC. A. Vlassov's simulation estimates a total hadronic rate of about 640 kHz at our proposed luminosity. Most of these particles will move forward and therefore miss our spectator cuts. Most of the pions will be above 100 MeV/c and deposit minimal charge in the RTPC. They can be easily distinguished from protons of similar stiffness by the huge difference in measured dE/dx, as discussed in the previous section (The same is true for heavier fragments, which will have much higher energy loss for the same stiffness.) Low momentum pions are unlikely to come from high momentum transfer interactions, i.e. they are not likely to be in true coincidence with the scattered electron, and can therefore excluded by timing and vertex cuts. Very low momentum pions will curl up in the solenoid field and not reach the recoil detector. At somewhat higher momenta (above 20 MeV/c), they can deposit a relatively large signal in the drift region of the TPC; however, they will be bent by a large angle in ϕ which can be easily detected using the azimuthal track length in the TPC. At momenta above 30 MeV/c, their energy loss in the active volume will be much smaller (by at least a factor of 3) than that of any of the protons of interest (VIPs).

The background contribution from entrance and exit window of the target can be suppressed by vertex cuts or subtracted using empty target runs. We will also use runs with hydrogen instead of deuterium as target gas to study additional background sources (as well as for calibration purposes).

The only significant background we expect is due to accidental coincidences between scattered electrons detected by CLAS12 and low-momentum protons liberated from the deuterium target by (nearly) real photons from the electron beam. These protons have similar momentum distribution and can be emitted in the backward direction, where they become indistinguishable from spectator protons (VIPs). The hadronic simulation mentioned above predicts a rate of about 160 kHz for these "VIP-like" protons, but in our experience, secondary interactions of (Møller or Rutherford-scattered) electrons as well as secondary photons and beam halo with the target and the target walls can produce a significantly higher low-momentum hadronic background. Therefore, we use our experience with the completed BoNuS experiment, where the uncorrelated proton rate in our RTPC was about 90 kHz, of which about 20 kHz mimicked "VIP-like" protons that passed all our cuts, for a luminosity of $0.5 \cdot 10^{33}$ cm^{-2}sec^{-1}. We assume that this rate depends only slightly on

beam energy (since most of these protons are produced by soft nearly-real photons) and therefore scale this rate by a factor of 40 to correspond with our planned luminosity of $2 \cdot 10^{34}$ cm^{-2}sec^{-1}. The resulting 800 kHz (within cuts) is significantly worse than predicted by the simulation, and we can use it as a reasonable "worst-case scenario" estimate.

We can reduce this rate substantially be applying a strict cut on the difference $\Delta z = z_{CLAS} - z_{RTPC}$ between the reconstructed vertices of the electron (detected by the CLAS12 forward tracker) and the spectator proton (detected by the RTPC). As shown in Section 6, the resolution achieved on Δz during the original BoNuS experiment was 8 mm. For the new experiment proposed here, we will be able to improve substantially on this resolution. First, the resolution of CLAS12 will be vastly better than that of CLAS (which dominated our existing result), since outgoing forward particles will be tracked in the forward vertex tracker. The anticipated resolution in z_{CLAS} is about 1-2 mm, according to the CLAS12 technical design report (TDR). Similarly, the RTPC resolution will also be much improved. The higher charge production rate in the new drift gas (Ne/DME) combined with the longer drift distance in the radially increased drift region will lead to many independent z-measurements by a large number of readout pads (at least 6 for the highest momentum tracks). Each measurement will have a resolution of about 1.4 mm (5 mm pad length divided by $\sqrt{12}$) and because of the stagger between adjacent pad rows, these measurements are largely independent. Taking the projection of the track back to the z-axis into account, the expected resolution should at least be 3 mm (see previous section), leading to an overall resolution for Δz of about 3.4 mm. Therefore, a cut of ± 5 mm will have about 86% efficiency and will exclude all but 1/40 of the total background rate, leaving about 20 kHz.

As the final step, we will apply a timing cut to select coincident proton tracks whenever an electron candidate is found. During the previous BoNuS experiment, this timing cut was set to 2 μs. This was necessary partially due to a rather large fluctuation of the cathode radius from point to point (most likely because of wrinkles introduced during assembly). The experience from eg6 shows that one can achieve wrinkle-free foils with the new assembly method. Assuming a spatial resolution of the track start and end points of about 2.5 mm (6% of the total track length of about 4 cm), we should be able to reduce the corresponding timing cut to less than 0.5μs (7% of the total expected drift time of about 7μs), yielding a probability of only 1% to detect an accidental "VIP-like" proton in coincidence with the electron. The true coincidence rate will be about 0.03 detected VIPs per electron, yielding an accidental/true ratio of about 1/3. This background can be easily quantified using the distribution of "VIP-like" tracks in time and in Δz and will be subtracted from the data. If the hadronic rate from the simulation is correct, the background will be five times smaller and become insignificant.

7.4 Systematic Errors

The size of various systematic error sources depends somewhat on the method employed to analyze our data. Following the route of the "main" BoNuS analysis (see Section 6), we divide the measured tagged rate for d$(e, e' p_s)$X by the inclusive d(e, e') rate and, after applying a few corrections and normalizing by the overall "VIP tagging efficiency", extract the ratio of structure functions, F_2^n / F_2^d. Using a model for F_2^d (well constrained to about 3% by the world data), the desired quantity F_2^n can be obtained. The advantage of this method

is that, to a large extent, experimental uncertainties (for instance on the CLAS12 acceptance and efficiency) cancel, and the model dependence is minimal. The disadvantage is that it assumes that the tagging efficiency (determined by normalizing F_2^n to the world data at low values of x where the nuclear model dependence is small) is independent of kinematics (x^*, Q^2). We tested this assumption with simulations of BoNuS, and found it to be true at below the 5% level (see Section 6.6) except at the edges of the kinematic acceptance, where the variation could be significant. (Fortunately, the high-x data we are most interested in are not at extreme values of electron momentum). Including the uncertainty on F_2^d, and possible bin migration and momentum smearing effects, the point-to-point systematic error specific to this analysis method alone is about 6-7% at the highest values of x and significantly lower at lower x.

We will cross check this method with the more detailed analysis described in Section 6.8 yielding a similar comparison as in Fig. 31, using a full simulation of the *combined* acceptance and efficiency of the forward tracker (CLAS or CLAS12) and the RTPC (implemented in GEANT4) to extract the structure function F_2^n directly from the data. This method has systematic errors stemming from our lack of precise knowledge of the detector response and efficiency, as well as some model dependence (due to bin migration effects) if the data simulated by the event generator are significantly different from the real data. Some of these uncertainties can be improved by using experimental input.

For instance, inclusive $d(e, e')$ and quasi-elastic $d(e, e'p)$ rates (with well-known cross sections) can be used to calibrate the CLAS12 acceptance and efficiency. Experience with the existing BoNuS data (where this method was used) show that one can get an overall point-to-point error on the electron acceptance times efficiency of about 5% or less using this method.

We will also use a dedicated run at 2.2 GeV to check and fine-tune our understanding of the RTPC acceptance and resolution, using the reaction $d(e, e'p\pi^- p_{spectator})$. By detecting the fast forward proton and the pion in CLAS12, we can predict the momentum of the spectator proton and if, according to our simulation, it was within the RTPC acceptance. The ratio of the number of spectator protons actually observed in the RTPC to that predicted by the simulation can be used to correct the RTPC efficiency empirically. In this context, it is important that the missing momentum of the spectator can be determined with sufficient resolution; a detailed study showed that the the uncertainty on its magnitude is about 15-20 MeV/c and on its angle about 6°. Again from experience with the existing BoNuS run, we are confident that this method will reduce the uncertainty on the RTPC acceptance times efficiency to less than 5%. The overall uncertainty specific to this method is thus about 7%. Comparing both methods should limit the point-to-point systematic error due to acceptance effects to 6% at most. Due to our normalization procedure, this error cancels at the lowest x values.

There are some more point-to-point systematic uncertainties common to both methods. As listed in Section 6.6, pion contamination and electrons from pair symmetric decays can be studied in detail and the corresponding uncertainty will be about 1%. The uncertainty on radiative corrections (away from the kinematic extremes where large elastic and quasi-elastic tails dominate) will be about 2%. Finally, the error due to background subtraction is mostly statistical (leading to an increase of the total statistical error by about 30% included in our predicted results), with a systematic error less than 3%. This systematic error is largely

independent of x and does not contribute more than 1-2% to the point-to-point error. The overall systematic error from all these sources, combined in quadrature to the one derived above, yields a point to point uncertainty of about 7% at the highest x.

Finally, several theoretical (model) uncertainties enter. The integrated probability of the deuteron wave function in momentum space over the acceptance of our detector from different microscopic models varies by less than 1%. This uncertainty is independent from kinematics and cancels after normalization. Extracting F_2 from measured cross sections requires knowledge of the longitudinal to transverse cross section ratio, R. This is discussed in detail in the following section; the corresponding uncertainty is about 2% (less at high x). The more important corrections come from deviations from the simple spectator picture, like breaking of factorization (less than 1%), remaining off-shell effects (up to 2% uncertainty at low x and perhaps 4% at the highest x) and final state interaction (3% to 5%, see Section 4). We can study these effects by subdividing our data into several bins of spectator momentum and angle and comparing them to data with higher spectator momenta (as taken by E6 and as will be available from the CLAS12 central tracker for any deuterium runs). Using the extrapolation method outlined towards the end of Section 4, we will be able to reduce the overall theoretical error to the order of 3-4% at the highest x (and correspondingly lower at moderate x). Our overall estimate of the combined systematic point-to-point error is therefore up to 8% at the highest x.

Note that the discussion above assumes that we will normalize our data to the (relatively well known) value of F_2^n in a region where nuclear effects are minimal (around $x = 0.1...0.3$). Therefore, uncertainties due to the total integrated luminosity (including effective target thickness) and other common factors (e.g., CLAS12 trigger and average detector inefficiencies) cancel completely. The cross normalization will yield an overall scale error of about 3-4% from the uncertainty on existing F_2^n parametrizations. Dividing by F_2^p to access the ratio d/u for $x \to 1$ may increase this scale error to 4-5%. Note that this scale error does *not* worsen the extrapolation from the last measured point in x to the limit $x = 1$, where the present uncertainty is $\pm 40\%$, compared to a 9% systematic error from the proposed experiment.

7.4.1 Sensitivity of F_2 Extraction on $R = \sigma_L/\sigma_T$

Extraction of the structure function F_2 from the measured cross section requires knowledge of the longitudinal to transverse cross section ratio, R. This experiment will not be capable of extracting both F_2 and R simultaneously, and will therefore have to make assumptions for the latter.

In the one photon exchange approximation, the cross section for unpolarized inclusive electron-nucleon scattering can be expressed in terms of the helicity coupling between the virtual photon and nucleon as

$$\frac{d\sigma}{d\Omega dE'} = \Gamma \left[\sigma_T(x, Q^2) + \epsilon\, \sigma_L(x, Q^2)\right], \tag{23}$$

where σ_T and σ_L are the photo-absorption cross sections for purely transverse and longitudinal virtual photons, respectively. Γ is the flux of transverse virtual photons and ϵ is the relative longitudinal flux, and are both purely kinematic factors. The F_2 structure function

is directly proportional to the double differential cross section at $\epsilon = 1$, i. e. $F_2 \propto \sigma_T + \sigma_L$, and at $\epsilon < 1$ the extraction of F_2 from cross section measurements depends on both ϵ and the contribution of longitudinal strength to the total cross section.

It can be easily shown that

$$F_2 \propto \frac{d\sigma}{d\Omega dE'} \cdot \frac{1+R}{1+\epsilon R}\,, \tag{24}$$

where $R(x, Q^2) \equiv \sigma_L/\sigma_T$. To estimate the sensitivity of extracting F_2 from BoNuS cross section measurements at a beam energy of 11 GeV we utilize Equation 24 and the R1990 [78] fit to both proton and deuteron measurements of R in the DIS. We note that a portion of the R1990 data set included kinematics overlapping with the proposed BoNuS DIS measurements and indicates that R for the deuteron is the same as R for the proton within the uncertainties. The percent difference of F_2 extracted from cross sections measurements utilizing R1990 and the estimated uncertainty in the fit (R1990 + dR1990) is shown in Figure 35 for electrons detected in CLAS at angles of 20, 30, and 40 degrees, and for $W < 1.8$ GeV. Note, that the latest design for the CLAS12 detector limits the electron scattering to a maximum of 35 degrees. It is observed that the average percent difference in this kinematic range is less than 2% and significantly smaller at the largest x values and most forward angles, where $\epsilon \rightarrow 1$ and the cross section measurements are directly proportional to F_2.

While precision measurements of R in the resonance region are currently lacking for both proton and deuteron targets at higher Q^2, there now exist precision measurements from Hall C on the proton for $Q^2 < 4.5$ GeV$^2/c^2$ [79], and for the first time duality is observed in both the longitudinal and transverse structure (and hence in R). In addition to the proton resonance region data, a program [80, 81] in Hall C took data, which will provide precision separations of the longitudinal and transverse cross sections for the deuteron in a kinematic region complementary to the proton measurements. Futhermore, it is expected that the continued development of global fits to the proton and deuteron longitudinal and transverse cross sections could further reduce the uncertainties on extracting F_2 from the proposed cross section measurements in the resonance region.

7.5 Expected Accuracy

We propose to collect 35 days (100% efficiency) of data on deuterium with 11 GeV beam and another six days on hydrogen. One of the days of hydrogen data taking should be carried out with a low energy electron beam of about 2.2 GeV. The 40 cm long target filled with 7.5 atm deuterium gas at room temperature and the 200 nA electron beam will yield a combined luminosity of about $2 \cdot 10^{34}$ cm^{-2}s^{-1}, about a factor of five below the standard CLAS12 luminosity.

Our simulation shows that under these conditions, we will collect a total of twenty million events with coincident detection of recoil protons below 100 MeV/c and above 110° relative to the $\mathbf{q}$ vector (VIPs) at 11 GeV. The average spectator light cone fraction will be $\alpha = 1.06$. We will cover a range in $W^\star$ from the elastic peak to about $W^\star = 4.5$ GeV and Q^2 from 1 to 14 GeV$^2/c^2$.

Inside our acceptance we expect to collect in 35 days of running a total of 150 million events, of which 120 million remain after cutting events with $W^\star > 2$ GeV.

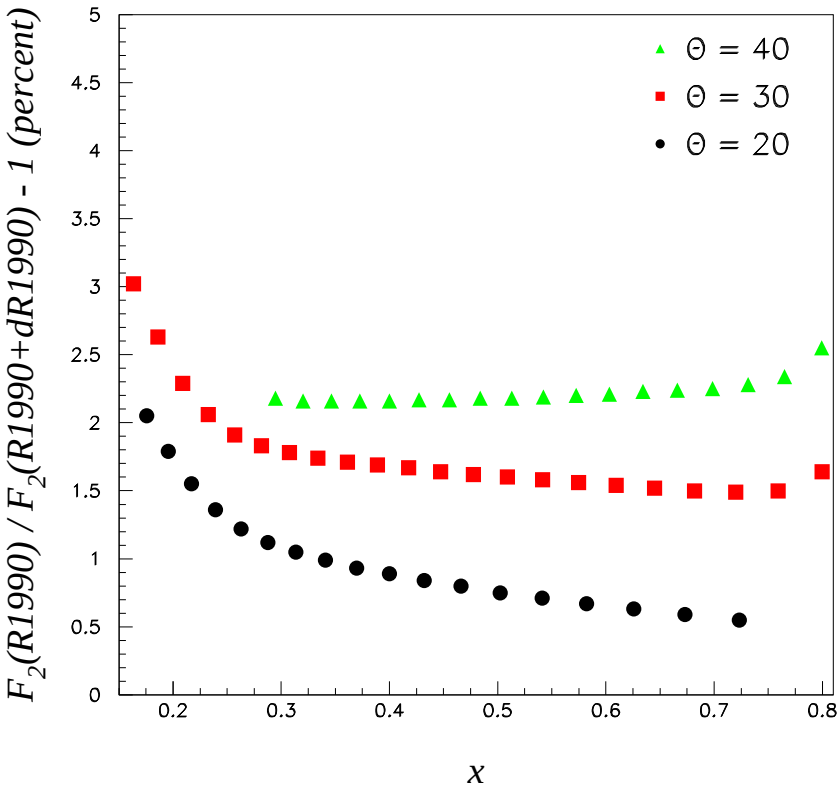

Figure 35: Percent difference between F_2 extracted from BoNuS cross section measurements utilizing the R1990 parameterization and the estimated uncertainty in the fit (R1990 + dR1990).

In Fig. 36, we show the kinematic range in Q^2 and x together with a cut of $W > 2$ GeV.

These new 11 GeV data will allow us to expand substantially the range in $x^\star$ over which the neutron structure function F_2^n is known with good statistical precision and with small theoretical uncertainties.

Fig. 37 shows the statistical precision we can achieve for the ratio F_2^n/F_2^p as a function of $x^\star$. The statistical error includes a 30% error contribution due to background subtraction. The curves at the bottom of the graph close to the x–axis indicates our estimate of the systematic error. The upper curve shows the total systematic error, from the combined experimental (acceptance, efficiency, event reconstruction, luminosity) and theoretical (deuteron wave function, off-shell and final state interaction effects) uncertainties. By normalizing our data to the well-known (and unambiguous) data at low x, we can extract the high–x behavior with much smaller uncertainty indicated by the lower curve.

The highest point in $x^\star$ which is still in the deep inelastic region $W^\star > 2$ GeV is at $x^\star = 0.76$, clearly in a region where valence quarks are dominant and existing data become uncertain because of nuclear effects. The present upper limit in $x^\star$ is below 0.6. If we extend these data to include $W^\star > 1.8$ GeV, we can add one more point in $x^\star = 0.81$ and also

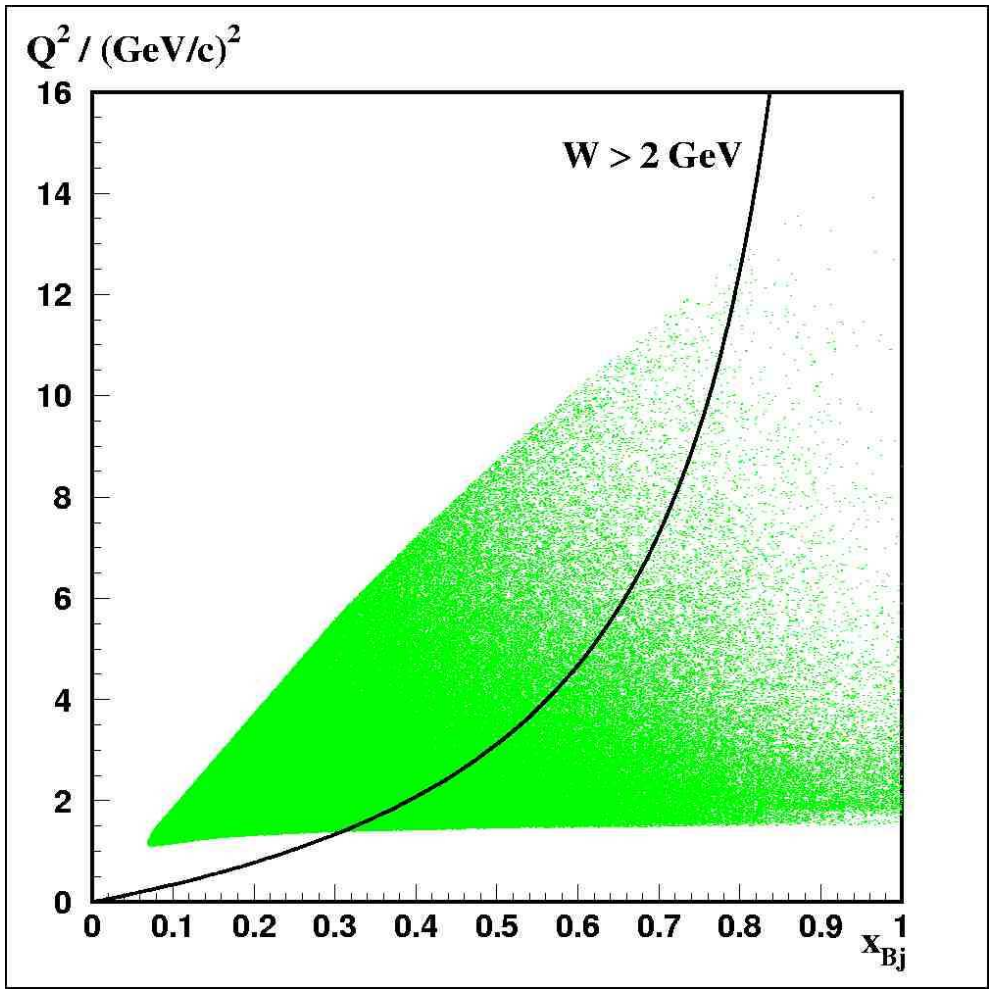

Figure 36: The kinematic range in Q^2 and x covered by this experiment, using the CLAS12 acceptance. The line correpsonds to $W = 2$ GeV.

significantly improve the statistical error on $x^\star = 0.76$. This is shown in Fig. 37 by the open square data points. At these high values of Q^2 (between 6 and 12 GeV$^2/c^2$) and $W^\star$, it is likely that duality is a very good approximation and we can interpret our results directly in terms of the ratio of d/u valence quark distributions. Of course, we will be able to test duality up to $x = 0.7$ over the whole range of Q^2 and $W^\star$ using our own data.

Clearly, the high precision data set indicated in Fig. 37 will allow a comprehensive study of the x and Q^2 dependence of the structure function F_2^n in the valence region, for the first time unclouded by uncertainties from nuclear binding effects.

The d/u ratio extracted from the same data are shown in Fig. 38. The systematic error curves at the bottom of the figure are due to the systematic error curves from Fig. 37. The lower curve represents the x-dependent point-to-point error, while the upper curve includes a 4% overall scale uncertainty.

The five days of data taking at 11 GeV with the hydrogen gas target will result in a measurement of F_2^p with the same acceptance and under the same beam conditions as the measurement with the deuterium gas target. The x-dependent point-to-point systematic

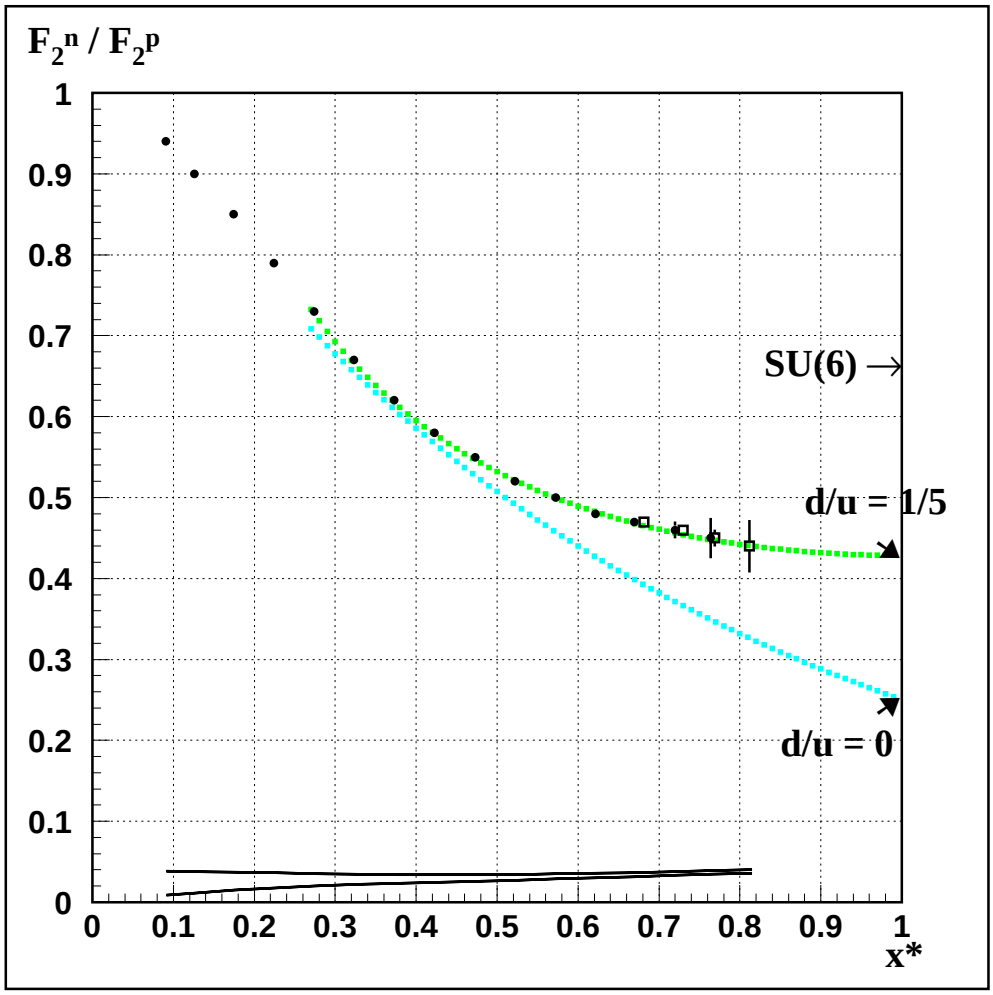

Figure 37: Ratio F_2^n/F_2^p versus $x^\star$ for spectator kinematics and $W^\star > 2$ GeV. The filled circle data points indicate the expected results of the proposed experiment with statistical error bars. The open squares data points show the improvement of the statistical error for a relaxed cut of $W^\star > 1.8$ GeV (the two lower $x^\star$ points are shifted slightly towards higher $x^\star$). The underlying coloured curves are duality based model calculations for different scenarios of SU(6) symmetry breaking from [21]. The naive SU(6) prediction for the $x^\star \to 1$ is indicated on the ordinate. The curves at the bottom of the figure indicates the estimated systematic error. The upper curve combines the experimental and theoretical uncertainties, while the lower curve represents the systematic error estimate due to experimental and theoretical uncertainties for the point-to-point error after normalization at low x.

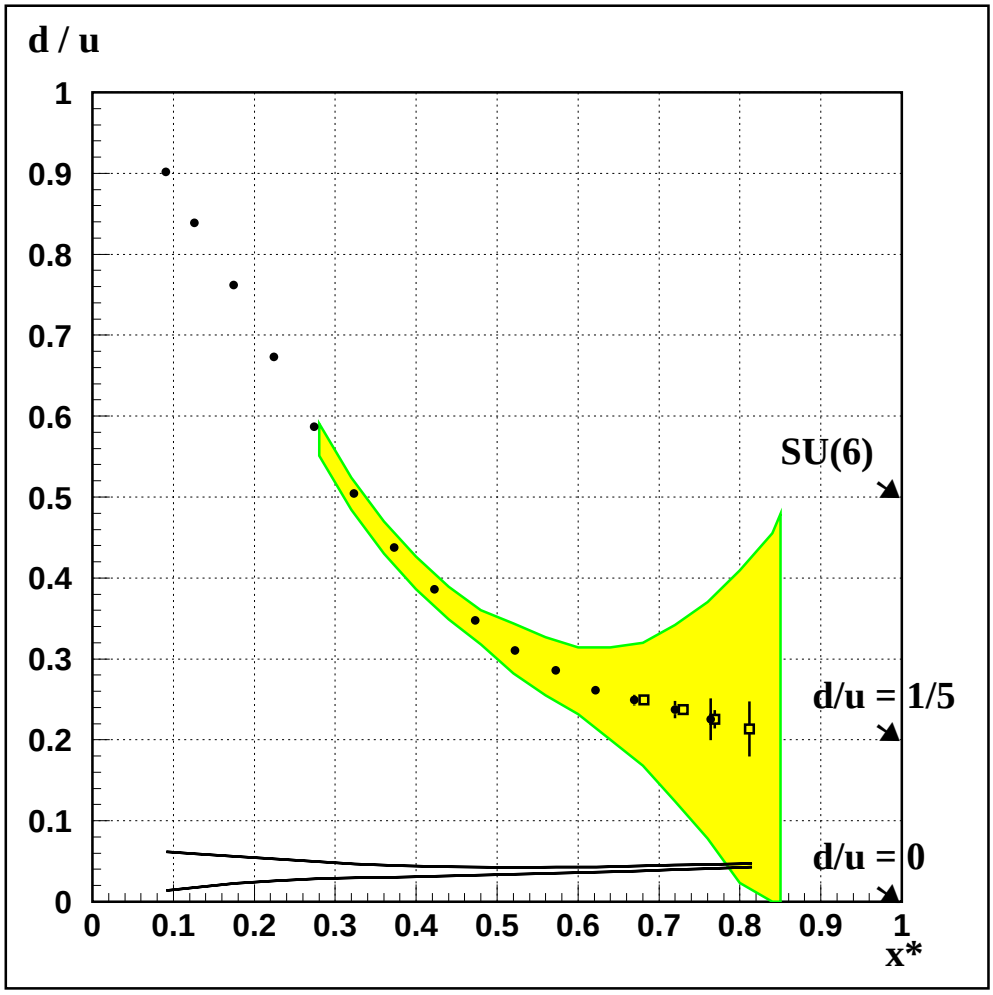

Figure 38: Ratio of d/u quarks versus $x^\star$ converted from the data points shown in Fig. 37. The upper and lower curves represent the systematic uncertainties due to the two systematic error curves as in Fig. 37. The shaded band indicates the present uncertainty in extracting the d/u ratio from the existing data.

uncertainity for the ratio F_2^d/F_2^p due to the RTPC acceptance will be reduced.

The data we plan to collect will also allow for quark–hadron duality studies in the neutron resonance region with very good precision. Measurements in the resonance region where carried out by experiment E03-012 and are being analyzed (see section 6).

Although the neutron resonance structure function and deep inelastic structure function data and parameterizations will obviously differ from the proton, we believe this is a good example of the potential quality of the neutron data attainable with BoNuS. This experiment will extend the Q^2 range and add statistics to the existing BoNuS measurement for $W < 2$ GeV as well as provide a more precise DIS structure function F_2^n to compare to.

Finally, we will also be able to contribute to the world's data set on elastic neutron form factors. The expected statistical and systematic errors for each measured Q^2 at $W = M_n$ are listed in Table 1. The systematic errors will be of order 6%. The present data from E94-017 extend to $Q^2 = 5$ GeV$^2/c^2$ with a statistical error of about 0.043 in the highest

Q^2-range / $(\mathrm{GeV}/c)^2$	No. of Events	Rel. Stat. Err.
2.0 – 2.5	16860	0.008
2.5 – 3.0	13332	0.009
3.0 – 3.5	7480	0.012
3.5 – 4.0	4000	0.016
4.0 – 4.5	2280	0.021
4.5 – 5.0	1460	0.026
5.0 – 6.0	1420	0.027
6.0 – 7.0	600	0.041
7.0 – 9.0	344	0.054

Table 1: Expected relative statistical error for the measurement of the normalized magnetic form factor of the neutron.

Q^2-bin. We can normalize our results at small Q^2, where good precision data are available, and can extract the elastic cross section with good accuracy at the higher Q^2, where we can compare our result with E94-017 up to $Q^2 = 5$ GeV$^2/c^2$ and extend the Q^2 range beyond (see Tab. 1). This will allow us to determine the absolute magnitude of the form factor G_M^n with a largely independent method.

7.6 Upgrade Possibilities for the RTPC

Depending on possible sources of funding, the readout speed of the RTPC could be further increased by changing the readout electronics. One option would be to change to a new chip, the APV25 [82], developed for the CMS collaboration at CERN's LHC and presently also under installation at the STAR detector at Brookhaven National Lab.

Currently, the CLAS trigger has a very high rate of events with no electrons in it. Some of us are proposing to develop a tracking trigger system based on FPGA technology, which would allow to improve the CLAS trigger rate by about a factor of two and dramatically reduce the background. This system would be based on the newly developed Amplifier Discriminator Boards (ADB) for CLAS12, which replace the old ADB boards as well as the FASTBUS TDC system. Since the BoNuS readout is driven by the CLAS trigger, such a trigger would greatly increase the data taking rate of BoNuS and at the same time enable experiments like nDVCS. In addition, such a tracking trigger would enable us to put vertex cuts into the trigger and greatly reduce background events from the target wall.

The collaborators from Los Alamos are working on resubmitting their tracking trigger proposal for Los Alamos National Lab (LANL) internal funding. Because of funding shortfalls this year it could not be funded, but they were encouraged to resubmit it for the next cycle. At the same time, the LANL management has been and is continuing to be very supportive of these efforts.

8 Summary and Beam Time Request

We propose to measure the structure function F_2^n of the neutron by scattering 11 GeV electrons off a deuterium gas target and detecting the scattered electron and recoiling proton. By selecting very backward scattering angles and very low recoil momenta for the proton, scattering events on almost free neutrons can be selected. This is particularly important at high x-Bjorken where Fermi motion effects in inclusive measurements are substantial.

For the detection of the recoil protons we propose to install a new and enlarged radial time projection chamber and target gas cell assembly, very similar to the ones used by the BoNuS (E03-012) and eg6 experiments. The RTPC can detect proton recoil momenta down to a lower limit of 70 MeV/c while being insensitive to minimum ionizing particles. We would use the upgraded CLAS12 forward spectrometer for electron and leading hadron detection.

The deep-inelastic scattering data, $W^\star > 2$ GeV, extend to $x^\star$ as high as 0.8, allowing for an extraction of the ratio F_2^n/F_2^p.

Comparing the data from the deep inelastic region extended to larger x with those from the resonance region, we can test duality for the neutron. The present proposal will increase the Q^2 range in the resonance region covered so far by experiment E03-012 and provide more statistics.

We request 35 days of 11 GeV beam using a deuterium gas target plus five days of 11 GeV beam using a hydrogen target. As demonstrated in the previous section, this will allow us to collect high precision data on the neutron and proton, with good statistics, resolution and kinematic coverage, and with minimal uncertainties due to nuclear binding effects. The beam time request was optimized to guarantee that the measurement is not statistics-limited. In addition, the statistical errors listed in the previous section assume that the whole data set for spectator momenta from 70 to 100 MeV/c will be integrated over. For most bins, the statistical precision will be good enough to allow us to study the dependence of the extracted structure functions on the spectator variables (momentum p_s, light cone fraction α and angle relative to the $\mathbf{q}$ vector).

In addition to the 40 days of data taking on deuterium and hydrogen we request one day of about 2.2 GeV beam for commissioning and calibration purposes, and 1 more day on an empty target for background studies.

Finally, we request resources from JLab to support the installation and integration into CLAS12 of the RTPC recoil detector. We also request support of JLab staff to support the integration of the RTPC readout into the new CLAS12 data acquisition software. Using our previous experience obtained during installation of experiment E03-012 we estimate that two weeks of setup time in the Hall will be needed for installation and comissioning of the target–detector system, including check-out without beam.

In total, we request 42 days of new beam time in Hall B for the program of neutron structure measurements described in this proposal, using the new CLAS12 detector.

References

[1] G. Dodge, *et al.*, *The Structure Function of the Free Neutron via Spectator Tagging*, JLab E03-012 Proposal to PAC23 (2003).

[2] N. Baillie, PhD thesis, *Electron Scattering from an Almost Free Neutron Target in Deuterium*, The College of William and Mary (2009).

[3] S. Tkachenko, *Neutron Structure Functions Measured with Spectator Tagging*, PhD thesis, Old Dominion University (2009).

[4] I. Aznauryan, *et al.*, JLab E07-009, www.jlab.org/exp_prog/proposals/07/PR07-009.pdf

[5] K. Hafidi, *et al.*, JLab E08-024, www.jlab.org/exp_prog/proposals/08/PR08-024.pdf

[6] R.P. Feynman, *Photon Hadron Interactions* (Benjamin, Reading, Massachusetts, 1972); F.E. Close, Phys. Lett. **B43**, 422 (1973); Nucl. Phys. **B80**, 269 (1973); R.D. Carlitz, Phys. Lett. **B58**, 345 (1975); N. Isgur, Phys. Rev. D **59**, 034013 (1999).

[7] A.D. Martin, R.G. Roberts, W.J. Stirling and R.S. Thorne, Eur. Phys. J. C **14**, 133 (2000); H.L. Lai, *et al.*, Eur. Phys. J. C **12**, 375 (2000); M. Glück, E. Reya and A. Vogt, Eur. Phys. J. C **5**, 461 (1998).

[8] G.R. Farrar and D.R. Jackson, Phys. Rev. Lett. **35**, 1416 (1975).

[9] L.W. Whitlow, *et al.*, Phys. Lett. B **282**, 475 (1992); A. Bodek, S. Dasu and S.E. Rock, in Tucson Part. Nucl. Phys., 768 (1991), SLAC-PUB-5598.

[10] W. Melnitchouk and A.W. Thomas, Phys. Lett. **B377**, 11 (1996).

[11] W. Melnitchouk and J.C. Peng, Phys. Lett. **B400**, 220 (1997).

[12] L.L. Frankfurt and M.I. Strikman, Nucl. Phys. **B250**, 1585 (1985); Phys. Rep. **160**, 235 (1988).

[13] I. Niculescu, *et al.*, Phys. Rev. Lett. **85**, 1186 (2000); I. Niculescu, *et al.*, Phys. Rev. Lett. **85**, 1182 (2000); R. Ent, C.E. Keppel and I. Niculescu, Phys. Rev. D **62**, 073008 (2000); S. Liuti, R. Ent, C.E. Keppel and I. Niculescu, Phys. Rev. Lett. **89**, 162001 (2002);

[14] J. Arrington, J. Crowder, R. Ent, C.E. Keppel and I. Niculescu, *Proceedings of the 9^{th} Int. Conf. on the Structure of Baryons 2002*, 550 (2002); J. Arrington, *et al.* Phys. Rev. C **64**, 014602 (2001).

[15] A. Airapetian, *et al.* (HERMES Collaboration), Phys. Rev. Lett. **90**, 092002 (2003);

[16] N. Isgur, S. Jeschonnek, W. Melnitchouk and J.W. Van Orden, Phys. Rev. D **65**, 054005 (2001); S. Jeschonnek and J.W. Van Orden, Phys. Rev. D **65**, 094038 (2002); V.V. Davidovsky and B.V. Struminsky, hep-ph/0205130; G. Ricco, M. Anghinolfi, M. Ripani, S. Simula and M. Taiuti, Phys. Rev. C **57**, 356 (1998).

[17] F.E. Close and N. Isgur, Phys. Lett. B **509**, 81 (2001).

[18] W. Melnitchouk, R. Ent and C.E. Keppel, Phys. Report **406**, 127 (2005).

[19] A. De Rujula, H. Georgi and H.D. Politzer, Ann. Phys. **103**, 315 (1977); H. Georgi and H.D. Politzer, Phys. Rev. D **14**, 1829 (1976).

[20] E.D. Bloom and F.J. Gilman, Phys. Rev. D **4**, 2901 (1970).

[21] F.E. Close and W. Melnitchouk, Phys. Rev. C **68**, 035210 (2003).

[22] S. P. Malace, Y. Kahn, W. Melnitchouk and C. E. Keppel, Phys. Rev. Lett. **104**, 102001 (2010).

[23] A. Accardi, M. E. Christy, C. E. Keppel, P. Monaghan, W. Melnitchouk, J. G. Morfin and J. F. Owens, Phys. Rev. D **81**, 034016 (2010).

[24] P. M. Nadolsky *et al.*, Phys. Rev. D **78**, 013004 (2008).

[25] A. D. Martin, W. J. Stirling, R. S. Thorne and G. Watt, Eur. Phys. J. C **63**, 189 (2009).

[26] S. Kuhlmann, *et al.*, Phys. Lett. B **476**, 291 (2000).

[27] W. Brooks, *et al.*, JLab E94-017, www.jlab.org/exp_prog/proposals/94/PR94-017.pdf

[28] J.D. Lachniet, *A high precision measurement of the neutron magnetic form factor using the CLAS detector*, Dissertation, Carnegie Mellon University (2005).

[29] J.D. Sullivan, Phys. Rev. D **5**, 1732 (1972).

[30] A. Thomas, Phys. Lett. B **126**, 97 (1983).

[31] P. Amaudruz, *et al.* (NMC), Phys. Rev. Lett. **66**, 2712 (1991); P. Amaudruz, *et al.* (NMC), Phys. Rev. D **50**, R1 (1994).

[32] K. Gottfried, Phys. Rev. Lett. **18**, 1174 (1967).

[33] A. Baldit, *et al.*, Phys. Lett. B **332**, 244 (1994).

[34] E.A. Hawker, *et al.* (E866 Collaboration), Phys. Rev. Lett. **80**, 3715 (1998).

[35] J.C. Peng, *et al.* (E866 Collaboration), Phys. Rev. D **58**, 092004 (1998).

[36] R.S. Towell, *et al.* (E866 Collaboration), Phys. Rev. D **64**, 052002 (2001).

[37] K. Akerstaff, *et al.* (HERMES Collaboration), Phys. Lett. B **464**, 123 (1999).

[38] C. Adloff, *et al.* (H1 Collaboration), Eur. Phys. J. **C6**, 587 (1999).

[39] P.M. King, *et al.*, Jefferson Lab Letter of Intent LOI-05-001 (2004).

[40] I.R. Afnan, *et al.*, Phys. Lett. B **493**, 36 (2000).

[41] K. Hafidi, *et al.*, Jefferson Lab Letter of Intent LOI12-10-009 (2010).

[42] R. Milner, *et al.*, Jefferson Lab Letter of Intent LOI12-10-008 (2010).

[43] L.L. Frankfurt and M.I. Strikman, Phys. Rep. **76**, 217 (1981).

[44] C. Ciofi degli Atti and S. Simula, Phys. Lett. **B319**, 23 (1993); Few-Body Systems **18**, 55 (1995); S. Simula, Phys. Lett. **B387**, 245 (1996); Few-Body Systems Suppl. **9**, 466 (1995).

[45] W. Melnitchouk, M. Sargsian and M.I. Strikman, Z. Phys. **A359**, 99 (1997).

[46] See e.g. R.P. Bickerstaff and A.W. Thomas, J. Phys. G **15**, 1523 (1989).

[47] S. Kulagin and R. Petti, Nucl. Phys. A **765**, 126 (2006).

[48] Y. Kahn, W. Melnitchouk and S. Kulagin, Phys. Rev. C **79**, 035205 (2009).

[49] W. Melnitchouk, A.W. Schreiber and A.W. Thomas, Phys. Lett. **B335**, 11 (1994); Phys. Rev. D **49**, 1183 (1994).

[50] G.D. Bosveld, A.E.L. Dieperink and A.G. Tenner, Phys. Rev. C **49**, 2379 (1994).

[51] F. Gross and S. Liuti, Phys. Rev. C **45**, 1374 (1992); S. Liuti and F. Gross, Phys. Lett. **B356**, 157 (1995).

[52] S.A. Kulagin, G. Piller and W. Weise, Phys. Rev. C **50**, 1154 (1994); S.A. Kulagin, W. Melnitchouk, G. Piller and W. Weise, Phys. Rev. C **52**, 932 (1995).

[53] S.I. Alekhin, S.A. Kulagin and S. Liuti, Phys. Rev. D **69**, 114009 (2004).

[54] L. Heller and A.W. Thomas, Phys. Rev. C **41**, 2756 (1990).

[55] S. Dieterich, *et al.*, Phys. Lett. **B500**, 47 (2001); R. Ransome, Nucl. Phys. **A699**, 360 (2002).

[56] W. Melnitchouk, K. Tsushima and A.W. Thomas, Eur. Phys. J. A **14**, 105 (2002).

[57] M. Sargsian and M. Strikman, Phys. Lett. B **639**, 223 (2006).

[58] L.L. Frankfurt, *et al.*, Z. Phys. **A352**, 97 (1995); Phys. Lett. **B369**, 201 (1996).

[59] C. Ciofi degli Atti and B.Z. Kopeliovich, Eur. Phys. J. A **17**, 133 (2003).

[60] M.I. Strikman, M. Tverskoy and M. Zhalov, nucl-th/9609055, *Proceedings of Workshop "Future Physics at HERA"*, Hamburg, 1085 (1996).

[61] M.R. Adams, *et al.*, Phys. Rev. Lett. **74**, 5198 (1995).

[62] B.Z. Kopeliovich, J. Nemchik and E. Predazzi, hep-ph/9511214, *Proceedings of the ELFE Summer School on Confinement Physics*, ed. S.D. Bass and P.A.M. Guichon, Editions Frontieres, Gif-sur-Yvette, 391 (1995).

[63] C. Ciofi degli Atti, L.P. Kaptari and D. Treleani, Phys. Rev. C **63**, 044601 (2001).

[64] C. Ciofi degli Atti, L.P. Kaptari and B.Z. Kopeliovich, Eur. Phys. J. A **19**, 145 (2004).

[65] F.E. Close, R.G. Roberts and G.G. Ross, Phys. Lett **B129**, 346 (1983).

[66] G.F. Chew and F.E. Low, Phys. Rev. **113**, 1640 (1959).

[67] H. Fenker, *et al.*, Nucl. Instrum. Meth. **A592**, 273 (2008).

[68] E. Elouadrhiri, *An Overview of the CLAS12 Spectrometer*, CLAS12 Document to PAC30 (2006).

[69] F. Sauli, Nucl. Instrum. Meth. **A386**, 531 (1997).

[70] L. Musa, *et al.*, Proc. of IEEE Nuclear Science Symposium 2003, Portland, USA (2003).

[71] P.E. Bosted and M.E. Christy, Phys. Rev. C **77**, 065206 (2008).

[72] M.E. Christy and P.E. Bosted, *Empirical Fit to Precision Inclusive Electron-Proton Cross Sections in the Resonance Region*, arXiv:0712.3731 (2007).

[73] N. Guler, *Pion and Pair Symmetric Contamination in the EG1B experiment*, CLAS technical note (*in progress*) (2010).

[74] L. Mo and Y. Tsai, Rev. Mod. Phys. **41**, 205 (1969).

[75] L.W. Whitlow *et al.*, Phys. Lett. **B282**, 475 (1992).

[76] J. Gomez *et al.*, Phys. Rev. D **49**, 4348 (1994).

[77] A.V. Klimenko, S.E. Kuhn, *et al.*, Phys. Rev. C **73**, 035212 (2006).

[78] L.W. Whitlow, *et al.*, Phys. Lett. B **250**, 193 (1990).

[79] Y. Liang, M.E. Christy, *et al.*, nucl-ex/0410027.

[80] M.E. Christy, *et al.*, JLab E02-109, www.jlab.org/exp_prog/proposals/02/PR02-109.ps

[81] J. Arrington, *et al.*, JLab E06-009, www.jlab.org/exp_prog/proposals/06/PR06-009.pdf

[82] R. Bainbridge, *et al.*, Nucl. Instrum. Meth. A **543**, 619 (2005).